Self-organized Toll-8/Cirl GPCR asymmetry drives planar polarized cell contractility

Jules Lavalou[1,4]*, Qiyan Mao[1]*, Stefan Harmansa[1,2], Stephen Kerridge[1], Annemarie C. Lellouch[1], Jean-Marc Philippe[1], Stephane Audebert[3], Luc Camoin[3], and Thomas Lecuit[1,2,4§]

1. IBDM-UMR7288, Aix Marseille Université and CNRS, Marseille, France.
2. Turing Centre for Living Systems, Marseille, France.
3. Centre de Recherche en Cancérologie de Marseille, Marseille Proteomics, Aix-Marseille Université, Inserm, CNRS, Institut Paoli Calmettes, Marseille, France
4. Collège de France, Paris, France.

* Equal contribution
§ Corresponding author: thomas.lecuit@univ-amu.fr

Abstract

Tissue morphogenesis requires spatial control over actomyosin contractility to drive cell shape changes[1,2]. How developmental patterning controls cell mechanics is poorly understood. In *Drosophila* embryos, Myosin-II is enriched at the interface between anteroposterior neighboring cells, driving planar polarized cell intercalation and extension of the embryonic axis[3–5]. G protein-coupled receptors (GPCRs) signaling controls Myosin-II activation at junctions[6,7] and Toll receptors provide a spatial bias to this process[8,9]. How Toll receptors polarize actomyosin contractility remains unknown. Here we report that cells expressing different levels of a single Toll receptor, Toll-8, activate Myosin-II at their interface. This does not require the intracellular domain of Toll-8, suggesting signaling by a proxy mechanism. We found that Toll-8 forms a molecular complex with the adhesion GPCR Cirl/Latrophilin that is required for junctional Myosin-II activation. We further show that Myosin-II is also activated at the interfaces between wild-type and *cirl* deficient cells. Since Toll-8 differentially recruits Cirl *in trans* and *in cis*, we propose that Toll-8 activates Myosin-II by inducing Cirl asymmetric localization at the boundary of its expression domain. Finally, we found that Toll-8 and Cirl exhibit dynamic interdependent planar polarization when neighboring cells express different levels of Toll-8. Through this feedback, Toll-8 and Cirl self-organize to drive planar polarized signaling. This work sheds new light on how embryo patterning induces cell polarization during morphogenesis.

During tissue morphogenesis, individual cells must coordinate their own polarity according to a global axis. In *Drosophila* embryos, maternally supplied morphogens gradients trigger a transcriptional cascade that defines periodic and partially overlapping stripes of Toll receptors perpendicular to the anteroposterior (AP) axis. Toll receptors are well known for their canonical function in developmental patterning and innate immunity[10], and have recently emerged as conserved molecules for cell surface recognition[10–15]. Each column of cells in the early *Drosophila* embryonic ectoderm expresses different combinations of Toll-2,6,8, which control

planar polarized Myosin-II (Myo-II) enrichment at interfaces between these columns[8,9]. However, it remains unclear how such a combinatorial code of cell surface molecules activates Myo-II.

Asymmetric expression of Toll-8 activates Myo-II

It has been hypothesized that *trans*-interactions between different Toll receptors signal to activate Myo-II[8]. In light of the observation that ectopic expression of Toll-2 or Toll-8 alone can induce Myo-II activation late in embryogenesis[8], we first tested the simplest hypothesis that a single Toll is sufficient to activate Myo-II in the embryonic ectoderm. To this end, we injected embryos with dsRNAs targeting Toll-2,6,7 (*toll-2,6,7* RNAi), leaving only endogenous Toll-8 expressed in vertical stripes (Extended Data Fig. 1a). We found Myo-II specifically enriched at the interfaces between Toll-8 expressing and non-expressing cells (Extended Data Fig. 1a, b), suggesting that Toll-8 alone can activate Myo-II.

To assess the signaling capacity of a single Toll in a more convincing manner, we engineered embryos expressing a single stripe of Toll-8 along the anteroposterior axis that runs orthogonal to the endogenous patterning stripes, using an *intermediate neuroblasts defective* (*ind*) enhancer[16] (*ind-Toll-8–HA*). We monitored Myo-II with GFP-tagged Myo-II regulatory light chain (MRLC–GFP) and detected Myo-II activation at the border between ectopic Toll-8 expressing and wild-type cells (Fig. 1a, b, Toll-8^{FL} and Extended Data Fig. 2a). Note that this ectopic Myo-II activation runs along the AP axis and is thus perpendicular to the endogenous planar polarity of Myo-II. When we deleted the Leucine-rich Repeats (LRRs) from the Toll-8 extracellular domain, Toll-8 no longer localized to the cell membrane and failed to activate Myo-II (Fig. 1a, b, Toll-$8^{\Delta LRR}$), suggesting that the LRRs of Toll-8 are essential for Myo-II activation. Consistent with an upregulation of cortical tension, the boundary of Toll-8 expressing cells was smoother when full-length Toll-8 (Toll-8^{FL}) was expressed compared to Toll-$8^{\Delta LRR}$ (Fig. 1a, c and Extended Data Fig. 2a, left).

When we injected *ind-Toll-8–HA* embryos with dsRNAs targeting only endogenous Toll-2,6,8 (*toll-2,6,8* RNAi), Myo-II was still activated at the boundary of ectopic Toll-8 expressing cells and formed a supracellular cable along the AP axis (Fig. 1d, e). This boundary was also smooth (Fig. 1d, f). Altogether, we conclude that an interface defined by a single Toll-8 is sufficient to activate Myo-II.

This led us to further dissect the mechanisms underlying the capacity of Toll-8 to elicit Myo-II activation using clonal analysis. We studied Toll-8 signaling in growing wing imaginal discs since clonal analysis is not possible in early embryos. Wing imaginal discs exhibit polarized supracellular cables of Myo-II at the periphery of the pouch region near the hinge[17]. Toll overexpression causes wing developmental defects[11] and Toll-8 is expressed in the wing hinge region but not in most of the pouch region[11,18]. We induced heat-shock clones overexpressing Toll-8–GFP in the larval wing disc epithelium, and monitored Myo-II localization with mCherry-tagged MRLC (MRLC–Ch) 24 hours after clone induction in the wing pouch. This resulted in a striking and robust planar polarized Myo-II activation specifically at the boundary of Toll-8 overexpressing clones (Toll-8^{FL}, Fig. 1g, h). As in embryos, we found that LRRs were required for Toll-8 plasma membrane localization and Myo-II activation in wing discs (Toll-$8^{\Delta LRR}$, Fig. 1g, h). Toll-8^{FL} clones were more compact with a smoother boundary compared

with Toll-8$^{\Delta LRR}$ clones (Fig. 1g, i and Extended Data Fig. 2a, right). The cytoplasmic domain of Toll proteins is necessary for canonical Toll signal transduction[10]. To test whether the cytoplasmic domain of Toll-8 is required for Myo-II activation, we generated wing disc clones overexpressing a truncated version of Toll-8, removing its cytoplasmic domain (Toll-8$^{\Delta Cyto}$). Surprisingly, Myo-II was still activated at the boundary of Toll-8$^{\Delta Cyto}$ overexpressing clones (Fig. 1g, h), and the clonal border was still smooth compared to Toll-8 $^{\Delta LRR}$ clones (Fig. 1g, i). We conclude that the cytoplasmic domain of Toll-8 is dispensable for Myo-II activation. This indicates that the signaling events leading to Myo-II activation at the border between Toll-8 expressing and non-expressing cells may require another protein presumably interacting with Toll-8 at the cell surface.

Toll-8 and Cirl form a molecular and functional complex

This led us to look for binding partners of Toll-8. To this end, we performed affinity purification-mass spectrometry using lysates isolated from embryos overexpressing Toll-8–YFP as a bait. Of the specifically bound proteins, Cirl was the most abundant target (Fig. 2a and Supplementary Table 1) and of particular interest, since it is the *Drosophila* homologue of vertebrate Latrophilin (Extended Data Fig. 3), a member of the adhesion G protein-coupled receptors (aGPCRs)[19,20]. Interestingly, the Toll-8 extracellular domain shares sequence similarities with the human LRRs protein FLRTs[21] (Extended Data Fig. 3), which are known to form a protein complex with human Latrophilin[22–25]. We also recovered Toll-2 as a significant Toll-8 target (Supplementary Table 1), in agreement with previous findings *in vitro*[8].

Using a Cirl–RFP knock-in line[26] to visualize endogenous Cirl, we found that Cirl localized to the membrane and was enriched at adherens junctions and in the subapical domain in both the embryo and the wing disc (Extended Data Fig. 4d-g). We next asked whether Cirl is required for Myo-II activation in the embryo. *cirl* maternal and zygotic mutant embryos showed delayed extension of the embryonic axis (Extended Data Fig. 4a-c) and a strong reduction of Myo-II at junctions in the ectoderm (Fig. 2b, c), resembling *toll-2,6,8* RNAi embryos (Fig. 2d and Extended Data Fig. 1a). We further tested whether Cirl is required for Toll-8-induced polarization of Myo-II. We analyzed the boundary of *ind-Toll-8–HA* stripe in wild-type and *cirl* null mutant embryos, and found a strong reduction of Myo-II activation and smoothness of the Toll-8 stripe in the absence of Cirl (Fig. 2e-g). Moreover, in wing imaginal discs we observed a similar reduction in Myo-II activation at the boundary of clones overexpressing Toll-8–YFP when *cirl* was null mutant (Fig. 2h, i). Note that Myo-II activation was not completely abolished, suggesting that other molecules in addition to Cirl mediate Toll-8-dependent polarization of Myo-II at cell interfaces. Taken together, we conclude that Toll-8 and Cirl form a molecular complex and interact functionally to polarize Myo-II at the interface of Toll-8 expressing and non-expressing cells.

Cirl asymmetric interfaces activate Myo-II

Interestingly, we observed that Myo-II was activated on both sides of the interface between Toll-8 expressing and non-expressing cells (Extended Data Fig. 5a, cyan arrowheads). This shows that Myo-II is also activated in cells that do not express Toll-8. We thus tested whether Cirl mediates signaling on both sides of the interface in a bidirectional manner. To this end, we

performed Mosaic Analysis with a Repressible Cell Marker (MARCM) in wing discs and induced *cirl* null mutant clones either adjacent to (Fig. 3a) or coincident with (Fig. 3b) Toll-8 overexpressing clones. We found that Myo-II was activated on both sides at the boundary of Toll-8 overexpressing clones when Cirl was mutant in neighboring cells (Fig. 3a, orange arrows and Extended Data Fig. 5a, orange arrowheads), as at control interfaces (Fig. 3a, cyan arrows and Extended Data Fig. 5a, cyan arrowheads). In addition, when Cirl was absent only within cells of Toll-8 overexpressing clones, Myo-II was still activated on both sides of the clonal boundary (Fig. 3b, magenta arrows and Extended Data Fig. 5b, magenta arrowheads). Thus, Cirl is dispensable either in Toll-8 expressing or in responding/contacting cells (Fig. 3c). This is remarkable since Cirl must be present on at least one side of Toll-8 overexpressing clones, as complete removal of Cirl on both sides reduces significantly Myo-II activation (Fig. 2h, i). We thus hypothesized that the role of Toll-8 is to induce an asymmetry of Cirl activity at the clonal boundary. To test this, we generated *cirl* mutant clones in the wing disc without overexpressing Toll-8. We reasoned that at the clonal interface Cirl activity is thereby *de facto* asymmetric. We found that Myo-II was indeed activated at the boundary of *cirl* mutant clones and that the boundary was smooth compared to control clones (Fig. 3d-f). This is similar to Toll-8 overexpressing clones, albeit to a lesser extent (Fig. 3a-e). We conclude that asymmetric Cirl interfaces can activate Myo-II and suggest that this underlies Toll-8-dependent planar polarization of Myo-II.

Toll-8 generates a Cirl interfacial asymmetry

One possible explanation is that the juxtaposition of Toll-8 expressing and no-expressing cells leads to Myo-II activation by inducing Cirl asymmetric localization at the clone boundary. To test this, we assessed the effect of Toll-8 overexpressing clones on endogenous Cirl localization in wing discs. In cells that do not overexpress Toll-8–YFP, Cirl–RFP was localized at adherens junctions and in the subapical domain (Extended Data Fig. 4f, g). However, in all Toll-8–YFP overexpressing cells, Cirl–RFP was expanded more apically (Extended Data Fig. 6a') and consistently colocalized with Toll-8–YFP (Fig. 4a and Extended Data Fig. 6a, a'), thus showing that Toll-8 relocalizes Cirl. We then used MARCM to look at Cirl–RFP only inside (Fig. 4b) or only adjacent to (Fig. 4c) Toll-8 overexpressing clones in order to assess Cirl localization on either sides of the clone boundary independently. When present only in Toll-8–YFP overexpressing cells (i.e. *in cis*), Cirl–RFP was relocated specifically to the apical surface at the clone boundary (Fig. 4b, d, arrow and Extended Data Fig. 6b). These results indicate that Toll-8 can recruit Cirl *in cis*. Strikingly, Cirl–RFP was also depleted from the orthogonal junctions in the first row of cells in direct contact with the clone boundary (Fig. 4a, arrows and Extended Data Fig. 6a), suggesting that Toll-8 also affects localization of Cirl in neighboring cells (i.e. *in trans*). When present only *in trans*, Cirl–RFP was planar polarized in cells in direct contact with the clone boundary and depleted from the junctions orthogonal to the clone border (Fig. 4c and Extended Data Fig. 6c), arguing that Toll-8 can recruit Cirl *in trans* too. In these cells, Cirl-RFP was relocalized specifically to the junctional plane together with E-cad (Fig. 4e, arrow). This *trans*-interaction did not require the presence of Cirl *in cis*, since Cirl–RFP was still relocalized *in trans* when *cirl* was removed inside Toll-8 overexpressing clones (Fig. 4f and Extended Data Fig. 6d). Since *in cis* Cirl is localized apically (Fig. 4d, arrow) while *in trans* it is recruited specifically to junctions (Fig. 4e, arrow), we conclude that Cirl is differentially localized between the two cell membranes at the Toll-8 clone boundary (Fig. 4g). When *cirl* is removed

inside Toll-8 overexpressing clones, the protein is still recruited *in trans* creating an asymmetry able to activate Myo-II (Figs. 3b, c and 4f). Taken together, these observations indicate that Toll-8 can induce an interfacial asymmetry of Cirl localization at its expression border. We propose that this interfacial asymmetry of Cirl is a key signal leading to Myo-II activation (Fig. 4g).

Toll-8 and Cirl form dynamic self-organized polarity patterns

In the previous experiments we monitored Toll-8, Cirl and Myo-II at least 24 hours following clone induction. The levels of Toll-8 expression were, as a result, very high. However, Myo-II planar polarization is an intrinsically dynamic and much faster process. To gain further insight into the process as it develops, we investigated the emergence of Toll-8-induced Myo-II activation in a dynamic context. We performed *ex vivo* live imaging[27] of nascent Toll-8 overexpressing clones in cultured wing discs. We used a temperature-sensitive GAL80 (GAL80ts) to precisely time the onset of Toll-8 expression by a temperature shift to 30°C. After 2h15 at 30°, we isolated wing discs with Toll-8–YFP clones and MRLC–mCherry and imaged them in a thermostatic chamber at 30°C. This allowed us to analyze Myo-II planar polarization as Toll-8 levels were low and as they increased over time. We took advantage of the fact that Toll-8 expression was not induced synchronously in all cells of a given clone, likely due to stochasticity in GAL80ts inactivation/GAL4 de-repression (Fig. 5a and Supplementary Videos 1-3). This led to the generation of stochastic and dynamic changes in Toll-8 expression and opened the possibility to correlate differences in Toll-8 expression levels and Myo-II planar polarization. We found that Myo-II was not only activated at the boundary of Toll-8–YFP expressing cells facing Toll-8–YFP negative cells consistent with previous experiments, but that Myo-II was also enriched at interfaces between cells with different Toll-8–YFP levels (Fig. 5a, Extended Data Fig. 7a and Supplementary Videos 1, 2). Moreover, as the levels of Toll-8–YFP increased, and once Toll-8–YFP expression reached the same level between these contacting cells, Myo-II enrichment was no longer sustained at the interface (Fig. 5a', arrowheads), and was stabilized only at the boundary of the clone (Fig. 5a, 330min and Extended Data Fig. 7a). This argues that stepwise differences in Toll-8 expression is sufficient to activate and polarize Myo-II.

Strikingly, we observed that Toll-8–YFP was initially planar polarized in low expressing cells and tended to accumulate at junctions facing away from the cells expressing higher levels of Toll-8–YFP (Fig. 5a, a', arrows and Supplementary Videos 1-3). Moreover, in cells where Toll-8–YFP was planar polarized, Myo-II was specifically activated at Toll-8-enriched junctions, leading to Myo-II planar polarity across several rows of cells (Fig. 5a, 110min and Supplementary Videos 1, 2). Therefore, Toll-8 polarization emerged when neighboring cells express different levels of Toll-8 and caused polarization of Myo-II.

We then asked how Cirl localization was affected by these nascent polarized patterns of Toll-8. Since Cirl–RFP was too low to be detected in our live imaging setup, we fixed wing discs treated under the same conditions. We found that Cirl–RFP was recruited to the interfaces where Toll-8 was planar polarized (Fig. 5b, arrows and Extended Data Fig. 7b). We conclude that Cirl forms planar polarized patterns in response to Toll-8 polarization. Finally, we asked if this transient Toll-8 planar polarity requires Cirl. To test this, we induced nascent Toll-8 overexpression clones in wild-type or *cirl* mutant wing discs by a temperature shift at 30° for

2h15. We found that Toll-8 planar polarity was strongly reduced in the absence of Cirl showing that Toll-8 and Cirl mutually attract each other in a dynamic manner (Fig. 5c, d).

Taken together, we propose a model in which Toll-8 expressing cells recruit Cirl at the boundary of Toll-8 expression and deplete it from orthogonal junctions in neighboring cells (Fig. 5e, panel 1). This generates Cirl planar polarity in these cells (Fig. 5e, panel 2). When Toll-8 expression is initiated in one of these neighbors, Toll-8 preferentially localizes to interfaces where Cirl is not depleted, thereby following Cirl polarity (Fig. 5e, panel 3). This new Toll-8-enriched interface will then recruit Cirl from orthogonal junctions, thus propagating Cirl planar polarity (Fig. 5e, panel 3). This process will continue until no new cells induce Toll-8 and converges on a stable pattern, where Toll-8 is expressed at uniformly high levels inside the clone and Cirl is planar polarized in one row of immediate neighbors (Fig. 5e, panel 4). We suggest that the spatial pattern and temporal sequence of Toll-8 expression translates into self-organized Toll-8/Cirl/Myo-II planar polarity due to local interactions between Toll-8 and Cirl (Fig. 5e).

Discussion

The interaction between Toll-8 and Cirl identified in our work documents a molecular and functional link between a Toll receptor and a GPCR. We show that Toll-8 asymmetric interfaces recruit Cirl differentially *in trans* and *in cis*, thus creating an interfacial Cirl asymmetry that activates Myosin-II. We further show that sequential expression of Toll-8 generates a scalar gradient, which drives Toll-8/Cirl planar polarity via feedback interactions across cell interfaces. Through this mechanism Toll-8 and Cirl can self-organize to drive planar polarized cell contractility.

Although clonal analysis is not possible in early *Drosophila* embryos, preventing the dissection of how a Cirl interfacial asymmetry might be generated in this tissue, we can propose two hypotheses on how several Toll receptors and Cirl may interact to define planar polarized interfaces for Myo-II activation. On the one hand, as Toll-2, 6 and 8 all have distinct expression patterns and boundaries in the embryo[8], and since Toll-8 alone is capable of polarizing Myo-II in embryos and discs, local Cirl asymmetry could be induced at each boundary independently, thereby allowing polarization on Myo-II at all interfaces on the basis of what we report here with Toll-8/Cirl[9]. Toll-2 or Toll-6 could function via Cirl or other proteins. On the other hand, interactions between different Toll receptors[8] (Supplementary Table 1) might modulate Toll-8/Cirl binding. This could lead to Cirl asymmetry at vertical interfaces across which different combinations of Toll receptors are expressed. How interfacial Cirl asymmetry may activate Myo-II remains unknown at the molecular level and likely involves yet other surface proteins, in particular other GPCRs such as Smog[6], with which Cirl could interact. The role of GPCRs and G protein signaling in conveying planar polarized input is substantiated by the observation that overexpression of heterotrimeric G protein subunits GβGγ, and to a lower extent p114RhoGEF, increases Myo-II planar polarization in early *Drosophila* embryos[7]. Cirl expression asymmetry may also induce Rho1 signaling and Myo-II activation without auxiliary protein in a manner akin to Cadherin2 at the interface between the neural tube and the epidermis in *Ciona*[28]. Cadherin2 homotypic binding recruits a RhoGAP and inhibits Rho1. The Cadherin2 +/- interfaces cannot recruit RhoGAP leading to Rho1 and Myo-II activation specifically at these interfaces. By analogy, Cirl +/- expression asymmetry (Fig. 3d), or localization and

functional asymmetry induced by Toll-8 (Figs. 4 and 5) may modulate Rho1 activation through regulation of RhoGAPs or RhoGEFs.

The depletion of Cirl observed around Toll-8 overexpressing cells resembles the effect of Flamingo (CELSR in vertebrates) overexpression on Frizzled localization[29,30], both central components of the conserved core Planar Cell Polarity (PCP) pathway[31]. Intriguingly, Flamingo is also an adhesion GPCR and shares sequence homology with Cirl[32]. It is also required for junctional Myo-II activation in early *Drosophila* embryos (data not shown). The *C. elegans* Cirl homologue LAT-1 aligns cell division planes to the embryonic AP axis[33]. The vertebrate Cirl homologue Latrophilin regulates synaptogenesis and neuronal migration via *trans*-heterophilic binding with FLRTs[22–25], which share sequence similarities with Toll-8 (Extended Data Fig. 3). FLRTs have been hypothesized to play a role in tissue morphogenesis[34,35]. The self-organized planar polarization of Toll-8/Cirl identified in our study suggests the possibility that GPCRs evolved different modalities of symmetry breaking. In the core PCP pathway, symmetry breaking is thought to happen through long range mechanical[36] or chemical gradients of adhesion molecules (Fat, Dachsous) or ligands (Wnt)[37]. In our case, a transcriptional scalar gradient of LRRs proteins provides an interfacial input capable of breaking symmetry. Through the interdependent association of Toll-8 and Cirl, quantitative (i.e. scalar) differences in Toll-8 induce Toll-8 and Cirl polarization. Thus, our work sheds new light on how positional information, which is encoded as concentrations of pair-rule genes such as *even-skipped*, is translated into vectorial cell interfacial information required for axis extension.

Author Contributions

J.L., Q.M. and T.L. conceived the project. Q.M., J.L. and S.K. performed experiments in embryos, Q.M analyzed them. J.L. performed all the experiments and data analysis in fixed wing discs. S.H. performed and analyzed live experiments in wing discs, and quantified data in Fig. 5d. Q.M. and A.L. prepared the samples for the mass spectrometry which was done and analyzed by S.A. and L.C. J-M.P. designed and generated the molecular constructs. J.L., Q.M. and T.L. wrote the manuscript and all authors made comments.

Acknowledgements

We thank all members of the Lecuit team, B. Aigouy (IBDM, France) for stimulating discussions during the course of this project, the IBDM imaging facility for microscopy assistance, FlyBase for maintaining curated databases and the Bloomington stock center for providing fly stocks. We thank T. Langenhan and N. Scholz (Leipzig, Germany) for sharing information about Cirl/Latrophilin and fly reagents, and for stimulating discussions. We thank B. Aigouy (IBDM, France) and P. Villoutreix (Centuri, France) for developing the method for quantifying clone smoothness in wing discs. We thank B. Habermann (IBDM, France) for her valuable guidance on performing pair-wise alignment between Toll-8 and FLRTs. We are grateful to M. Ludwig (Birmingham, UK), P.F. Lenne (IBDM, France), E. Wieschaus (Princeton, USA), A. Martin (MIT, USA), R. Karess (IJM, France), G. Jiménez (IBMB, Spain) and T. Gregor (Pasteur Institute, France) for the gift of flies and vectors. This work was supported by grants from the ERC (Biomecamorph no. 323027) and the Ligue Nationale Contre le Cancer (Equipe Labellisée 2018). J.L. was supported by the Fondation Bettencourt Schueller and the Collège de France. S.H. was supported by an EMBO Long-Term Fellowship (EMBO ALTF 217-2017) and by a Centuri Postdoctoral Fellowship (Centuri, France). The Marseille Proteomics (IBiSA) is supported by Institut Paoli-Calmettes (IPC) and Canceropôle PACA. Proteomics analysis was supported by the Institut Paoli-Calmettes and the Centre de Recherche en Cancérologie de Marseille. Proteomic analyses were done using the mass spectrometry facility of Marseille Proteomics (marseille-proteomique.univ-amu.fr) supported by IBISA (Infrastructures Biologie Santé et Agronomie), Plateforme Technologique Aix-Marseille, the Cancéropôle PACA, the Provence-Alpes-Côte d'Azur Région, the Institut Paoli-Calmettes and the Centre de Recherche en Cancérologie de Marseille. We acknowledge the France-BioImaging infrastructure supported by the French National Research Agency (ANR–10–INBS-04-01, Investments for the future).

Competing financial interests

The authors declare no competing financial interests.

References

1. Munjal, A. & Lecuit, T. Actomyosin networks and tissue morphogenesis. *Development* **141**, 1789–1793 (2014).

2. Devenport, D. Tissue morphodynamics: Translating planar polarity cues into polarized cell behaviors. *Seminars in Cell and Developmental Biology* **55**, 99–110 (2016).

3. Irvine, K. D. & Wieschaus, E. Cell intercalation during Drosophila germband extension and its regulation by pair-rule segmentation genes. *Development* **120**, 827–841 (1994).

4. Bertet, C., Sulak, L. & Lecuit, T. Myosin-dependent junction remodelling controls planar cell intercalation and axis elongation. *Nature* **429**, 667–71 (2004).

5. Zallen, J. A. & Wieschaus, E. Patterned gene expression directs bipolar planar polarity in Drosophila. *Dev. Cell* **6**, 343–355 (2004).

6. Kerridge, S. *et al.* Modular activation of Rho1 by GPCR signalling imparts polarized myosin II activation during morphogenesis. *Nat. Cell Biol.* (2016).

7. Garcia De Las Bayonas, A., Philippe, J. M., Lellouch, A. C. & Lecuit, T. Distinct RhoGEFs Activate Apical and Junctional Contractility under Control of G Proteins during Epithelial Morphogenesis. *Curr. Biol.* **29**, 3370-3385.e7 (2019).

8. Paré, A. C. *et al.* A positional Toll receptor code directs convergent extension in Drosophila. *Nature* **515**, 523–527 (2014).

9. Tetley, R. J., Blanchard, G. B., Fletcher, A. G., Adams, R. J. & Sanson, B. Unipolar distributions of junctional myosin II identify cell stripe boundaries that drive cell intercalation throughout drosophila axis extension. *Elife* **5**, 1–35 (2016).

10. Anthoney, N., Foldi, I. & Hidalgo, A. Toll and Toll-like receptor signalling in development. *Development* 1–6 (2018).

11. Yagi, Y., Nishida, Y. & Ip, Y. T. Functional analysis of Toll-related genes in Drosophila. *Dev. Growth Differ.* **52**, 771–783 (2010).

12. Paré, A. C. *et al.* An LRR Receptor-Teneurin System Directs Planar Polarity at Compartment Boundaries. *Dev. Cell* **51**, 208-221.e6 (2019).

13. Ward, A., Hong, W., Favaloro, V. & Luo, L. Toll receptors instruct axon and dendrite targeting and participate in synaptic partner matching in a drosophila olfactory circuit. *Neuron* **85**, 1013–1028 (2015).

14. Benton, M. A. *et al.* Toll Genes Have an Ancestral Role in Axis Elongation. *Curr. Biol.* **26**, 1609–1615 (2016).

15. Meyer, S. N. *et al.* An ancient defense system eliminates unfit cells from developing tissues during cell competition. *Science* **346**, (2014).

16. Stathopoulos, A. & Levine, M. Localized repressors delineate the neurogenic ectoderm in the early Drosophila embryo. *Dev. Biol.* **280**, 482–493 (2005).

17. LeGoff, L., Rouault, H. & Lecuit, T. A global pattern of mechanical stress polarizes cell divisions and cell shape in the growing *Drosophila* wing disc. *Development* **140**, 4051–4059 (2013).

18. Alpar, L., Bergantiños, C. & Johnston, L. A. Spatially Restricted Regulation of

Spätzle/Toll Signaling during Cell Competition. *Dev. Cell* **46**, 706-719.e5 (2018).

19. Scholz, N. *et al.* The Adhesion GPCR Latrophilin/CIRL Shapes Mechanosensation. *Cell Rep.* **11**, 866–874 (2015).

20. Schöneberg, T. & Prömel, S. Latrophilins and Teneurins in Invertebrates: No Love for Each Other? *Front. Neurosci.* **13**, 1–11 (2019).

21. Dolan, J. *et al.* The extracellular Leucine-Rich Repeat superfamily; a comparative survey and analysis of evolutionary relationships and expression patterns. *BMC Genomics* **8**, 320 (2007).

22. O'Sullivan, M. L. *et al.* FLRT Proteins Are Endogenous Latrophilin Ligands and Regulate Excitatory Synapse Development. *Neuron* **73**, 903–910 (2012).

23. Boucard, A. A., Maxeiner, S. & Südhof, T. C. Latrophilins function as heterophilic cell-adhesion molecules by binding to teneurins: regulation by alternative splicing. *J. Biol. Chem.* **289**, 387–402 (2014).

24. Sando, R., Jiang, X. & Südhof, T. C. Latrophilin GPCRs direct synapse specificity by coincident binding of FLRTs and teneurins. *Science* **363**, eaav7969 (2019).

25. del Toro, D. *et al.* Structural Basis of Teneurin-Latrophilin Interaction in Repulsive Guidance of Migrating Neurons. *Cell* **180**, 323-339.e19 (2020).

26. Scholz, N. *et al.* Mechano-dependent signaling by latrophilin/CIRL quenches cAMP in proprioceptive neurons. *Elife* **6**, (2017).

27. Dye, N. A. *et al.* Cell dynamics underlying oriented growth of the drosophila wing imaginal disc. *Development* **144**, 4406–4421 (2017).

28. Hashimoto, H. & Munro, E. Differential Expression of a Classic Cadherin Directs Tissue-Level Contractile Asymmetry during Neural Tube Closure. *Dev. Cell* **51**, 158-172.e4 (2019).

29. Chen, W. S. *et al.* Asymmetric Homotypic Interactions of the Atypical Cadherin Flamingo Mediate Intercellular Polarity Signaling. *Cell* **133**, 1093–1105 (2008).

30. Strutt, H. & Strutt, D. Differential Stability of Flamingo Protein Complexes Underlies the Establishment of Planar Polarity. *Curr. Biol.* **18**, 1555–1564 (2008).

31. Devenport, D. Cell biology in development: The cell biology of planar cell polarity. *J. Cell Biol.* **207**, 171–179 (2014).

32. Langenhan, T., Aust, G. & Hamann, J. Sticky signaling--adhesion class G protein-coupled receptors take the stage. *Sci Signal* **6**, re3 (2013).

33. Langenhan, T. *et al.* Latrophilin Signaling Links Anterior-Posterior Tissue Polarity and Oriented Cell Divisions in the C. elegans Embryo. *Dev. Cell* **17**, 494–504 (2009).

34. Karaulanov, E. E., Böttcher, R. T. & Niehrs, C. A role for fibronectin-leucine-rich transmembrane cell-surface proteins in homotypic cell adhesion. *EMBO Rep.* **7**, 283–90 (2006).

35. Smith, T. G. & Tickle, C. The expression of Flrt3 during chick limb development. *Int. J. Dev. Biol.* **50**, 701–4 (2006).

36. Aigouy, B. *et al.* Cell Flow Reorients the Axis of Planar Polarity in the Wing

Epithelium of Drosophila. *Cell* **142**, 773–786 (2010).

37. Aw, W. Y. & Devenport, D. Planar cell polarity: Global inputs establishing cellular asymmetry. *Current Opinion in Cell Biology* (2016).

38. Huang, J., Zhou, W., Dong, W., Watson, A. M. & Hong, Y. From the Cover: Directed, efficient, and versatile modifications of the Drosophila genome by genomic engineering. *Proc. Natl. Acad. Sci. U. S. A.* **106**, 8284–8289 (2009).

39. Ludwig, M. Z., Manu, Kittler, R., White, K. P. & Kreitman, M. Consequences of eukaryotic enhancer architecture for gene expression dynamics, development, and fitness. *PLoS Genet.* (2011).

40. Chan, E. H. Y., Shivakumar, P. C., Clément, R., Laugier, E. & Lenne, P. F. Patterned cortical tension mediated by N-cadherin controls cell geometric order in the drosophila eye. *Elife* **6**, 1–27 (2017).

41. Martin, A. C., Kaschube, M. & Wieschaus, E. F. Pulsed contractions of an actin-myosin network drive apical constriction. *Nature* **457**, 495–9 (2009).

42. Bischof, J., Maeda, R. K., Hediger, M., Karch, F. & Basler, K. An optimized transgenesis system for Drosophila using germ-line-specific φC31 integrases. *Proc. Natl. Acad. Sci. U. S. A.* **104**, 3312–3317 (2007).

43. Bothma, J. P. *et al.* Dynamic regulation of eve stripe 2 expression reveals transcriptional bursts in living Drosophila embryos. *Proc. Natl. Acad. Sci. U. S. A.* **111**, 10598–10603 (2014).

44. Lim, B. *et al.* Kinetics of gene derepression by ERK signaling. *Proc. Natl. Acad. Sci.* **110**, 10330–10335 (2013).

45. Shevchenko, A., Wilm, M., Vorm, O. & Mann, M. Mass spectrometric sequencing of proteins from silver-stained polyacrylamide gels. *Anal. Chem.* (1996). doi:10.1021/ac950914h

46. Cox, J. *et al.* Accurate proteome-wide label-free quantification by delayed normalization and maximal peptide ratio extraction, termed MaxLFQ. *Mol. Cell. Proteomics* (2014).

47. Cox, J. & Mann, M. MaxQuant enables high peptide identification rates, individualized p.p.b.-range mass accuracies and proteome-wide protein quantification. *Nat. Biotechnol.* (2008).

48. Vizcaíno, J. A. *et al.* ProteomeXchange provides globally coordinated proteomics data submission and dissemination. *Nat. Biotechnol.* **32**, 223–226 (2014).

49. Bailles, A. *et al.* Genetic induction and mechanochemical propagation of a morphogenetic wave. *Nature* **572**, 467–473 (2019).

50. Müller, H.-A. J. Immunolabeling of Embryos. in *Drosophila* (ed. Dahmann, C.) **420**, 207–218 (Humana Press, 2008).

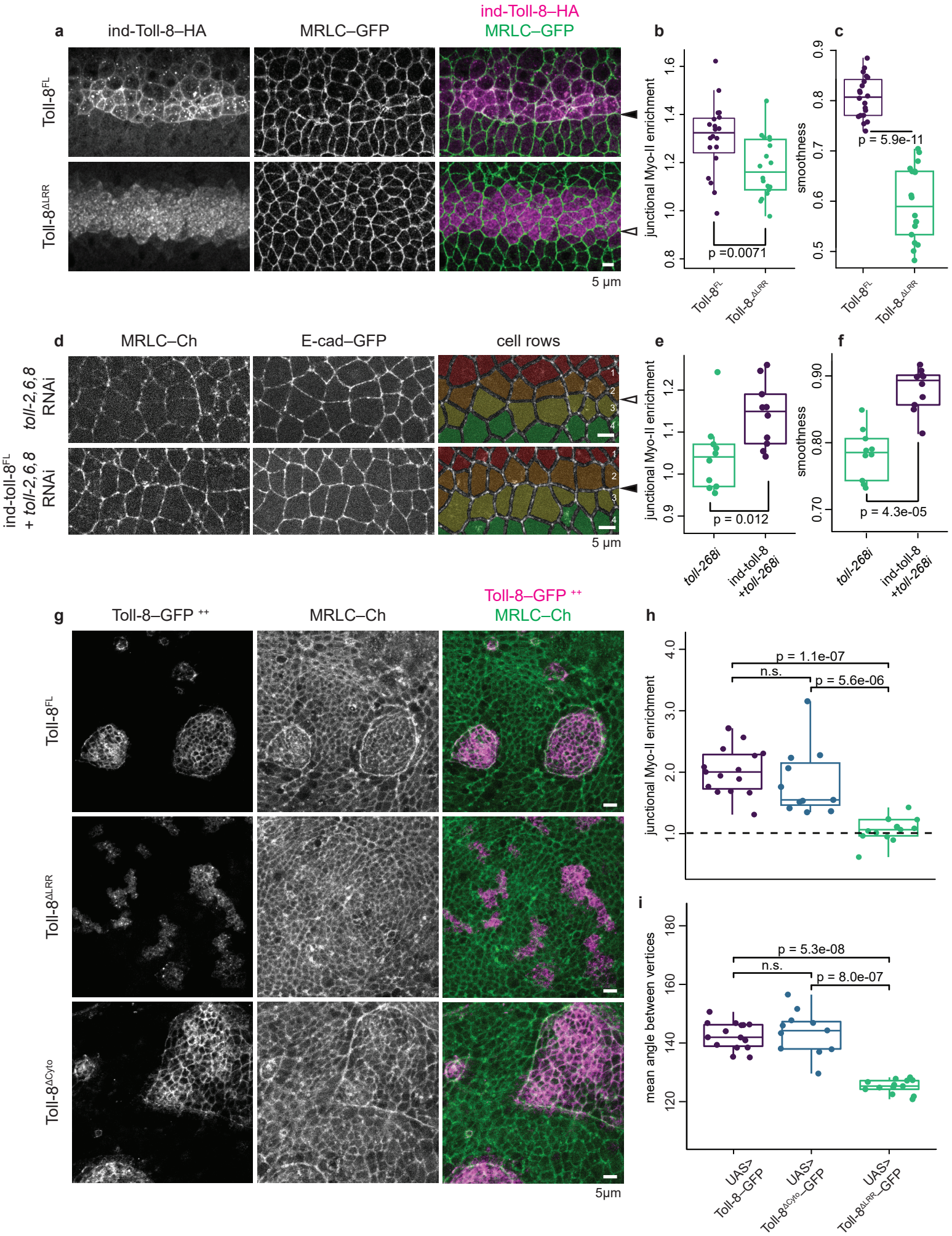
a
ind-Toll-8–HA
MRLC–GFP
ind-Toll-8–HA
MRLC–GFP
Toll-8FL
Toll-8ΔLRR
5 µm
b
junctional Myo-II enrichment
p =0.0071
Toll-8FL
Toll-8-ΔLRR
c
smoothness
p = 5.9e-11
Toll-8FL
Toll-8-ΔLRR
d
MRLC–Ch
E-cad–GFP
cell rows
toll-2,6,8 RNAi
ind-toll-8FL + toll-2,6,8 RNAi
5 µm
e
junctional Myo-II enrichment
p = 0.012
toll-268i
ind-toll-8 +toll-268i
f
smoothness
p = 4.3e-05
toll-268i
ind-toll-8 +toll-268i
g
Toll-8–GFP ++
MRLC–Ch
Toll-8–GFP ++
MRLC–Ch
Toll-8FL
Toll-8ΔLRR
Toll-8ΔCyto
5µm
h
junctional Myo-II enrichment
p = 1.1e-07
n.s.
p = 5.6e-06
i
mean angle between vertices
p = 5.3e-08
n.s.
p = 8.0e-07
UAS> Toll-8–GFP
UAS> Toll-8ΔCyto–GFP
UAS> Toll-8ΔLRR–GFP

Figure 1

Fig. 1 | Toll-8 activates Myo-II at the boundary of its expression domain, independent of its cytoplasmic tail. a, Anti-Toll-8–HA (left) and anti-MRLC-GFP (middle) signals in *Drosophila* stage 7 embryos expressing full length Toll-8 (Toll-8^{FL}, top, *n*=20) or Toll-8 with the extracellular LRRs removed (Toll-$8^{\Delta LRR}$, bottom, *n*=18) under the *ind* promoter. Myo-II is activated at the ventral border of the ind-Toll-8^{FL}–HA expression domain (filled arrowhead) but not in the ind-Toll-$8^{\Delta LRR}$–HA (empty arrowhead). **b, c,** Junctional Myo-II enrichment (**b**) and boundary smoothness (**c**) are quantified at the ventral *ind* boundary for the conditions shown in (**a**). **d,** Still images from time lapse movies (left) in *wt* embryos (top) or embryos expressing ind-Toll-8^{FL}–HA (bottom) injected with dsRNAs against Toll-2,6,8 (*n*=10 each). Pseudo colors mark 4 horizontal cell rows (right). Myo-II is still activated at the interface between cell rows 2 and 3 corresponding to the *ind* ventral boundary in the absence of endogenous Toll-2,6,8 (filled arrowhead). **e, f,** Junctional Myo-II enrichment (**e**) and boundary smoothness (**f**) are quantified at the ventral *ind* boundary for the conditions shown in (**d**). **g,** Fixed Toll-8–GFP (left) and MRLC–Ch (middle) signals from wing disc clones overexpressing full length Toll-8 (Toll-8^{FL}, top, *n*=15), Toll-8 with the extracellular LRRs removed (Toll-$8^{\Delta LRR}$, middle, *n*=11), or Toll-8 with the intracellular cytoplasmic tail removed (Toll-$8^{\Delta Cyto}$, bottom, *n*=13). Myo-II activation requires the extracellular LRRs but not the cytoplasmic tail of Toll-8. **h, i,** Junctional Myo-II enrichment (**h**) and boundary smoothness (**i**) are quantified at clone boundaries for the conditions shown in (**g**). Scalebars: 5 µm. n.s.: $p > 0.05$; Mann-Whitney U test.

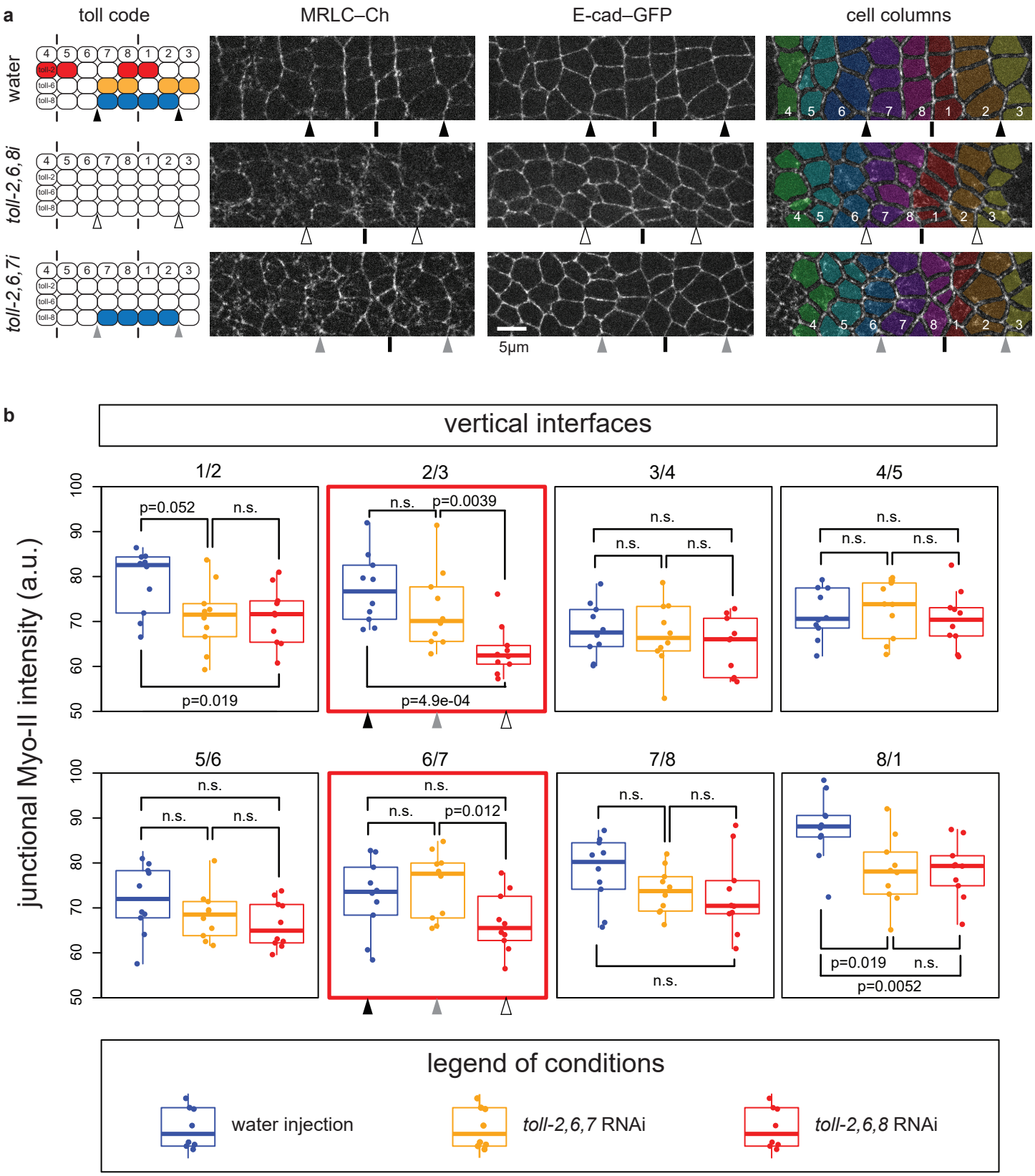
a
toll code
MRLC–Ch
E-cad–GFP
cell columns
water
toll-2,6,8i
toll-2,6,7i
5µm
b
vertical interfaces
junctional Myo-II intensity (a.u.)
1/2
2/3
3/4
4/5
5/6
6/7
7/8
8/1
p=0.052
n.s.
p=0.019
p=0.0039
p=4.9e-04
p=0.012
legend of conditions
water injection
toll-2,6,7 RNAi
toll-2,6,8 RNAi

Extended Data Fig. 1 | Endogenous Toll-8 is able to enrich Myo-II at its expression boundaries independent of Toll-2,6 (related to Fig. 1). a, Schematics showing the Toll code composed of Toll-2,6,8 expression in embryos (left). Still images from time lapse movies of embryos injected with water (top), dsRNAs against Toll-2,6,8 (middle) and dsRNAs against Toll-2,6,7 (bottom). Pseudo colors represent cell columns (right). Cell columns 1-4 belong to odd-numbered parasegments demarked with Even-skipped expression, while 5-8 belong to even-numbered parasegments. In all panels, vertical dashes represent parasegment boundaries where Myo-II is activated despite of Toll-2,6,8 knockdowns. Arrowheads demark boundaries of the Toll-8 expression domain in embryos injected with water (black), dsRNAs against Toll-2,6,8 (white) or Toll-2,6,7 (grey), where Myo-II is activated in the sole presence of Toll-8 (bottom). **b,** Quantifications of junctional Myo-II levels at indicated interfaces in embryos injected with water (blue, n=10), dsRNAs against Toll-2,6,7 (orange, n=10) and dsRNAs against Toll-2,6,8 (red, n=10). Black, white and grey arrowheads show quantifications of interfaces highlighted in (**a**). Scalebars: 5 µm. n.s.: $p > 0.05$; Mann-Whitney U test.

a

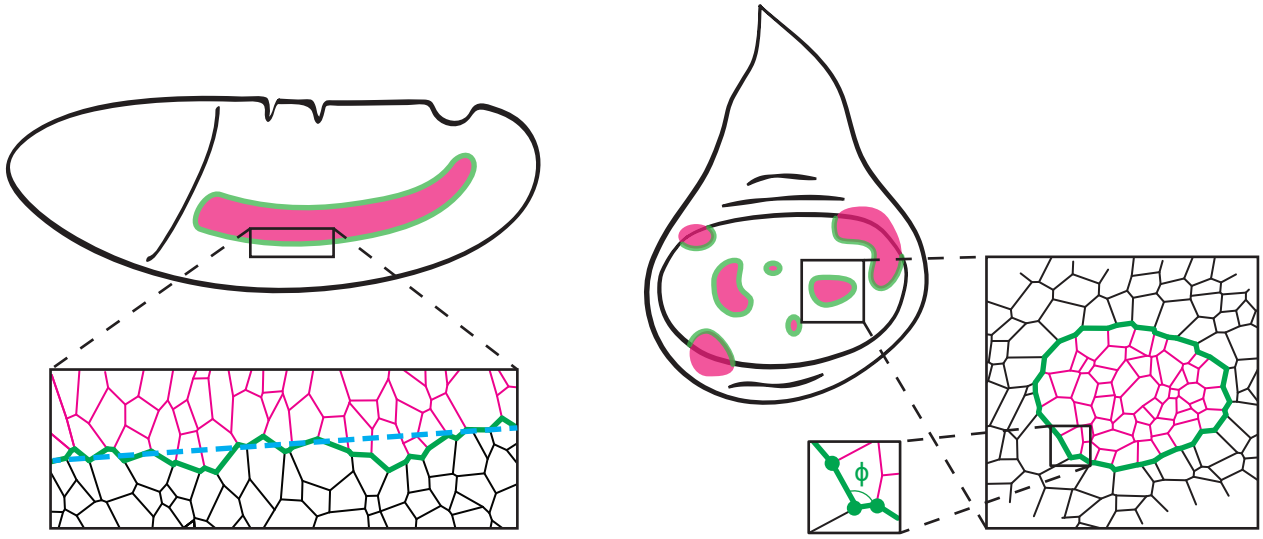

Myo-II enrichment = $\frac{\text{mean(border junction Myo-II intensity)}}{\text{mean(wt junction Myo-II intensity)}}$

smoothness (embryo) = $\frac{\text{distance between ending vertices}}{\text{total length interface junctions}}$

smoothness (wing disc) = mean(angle ϕ between neighboring vertices)

b

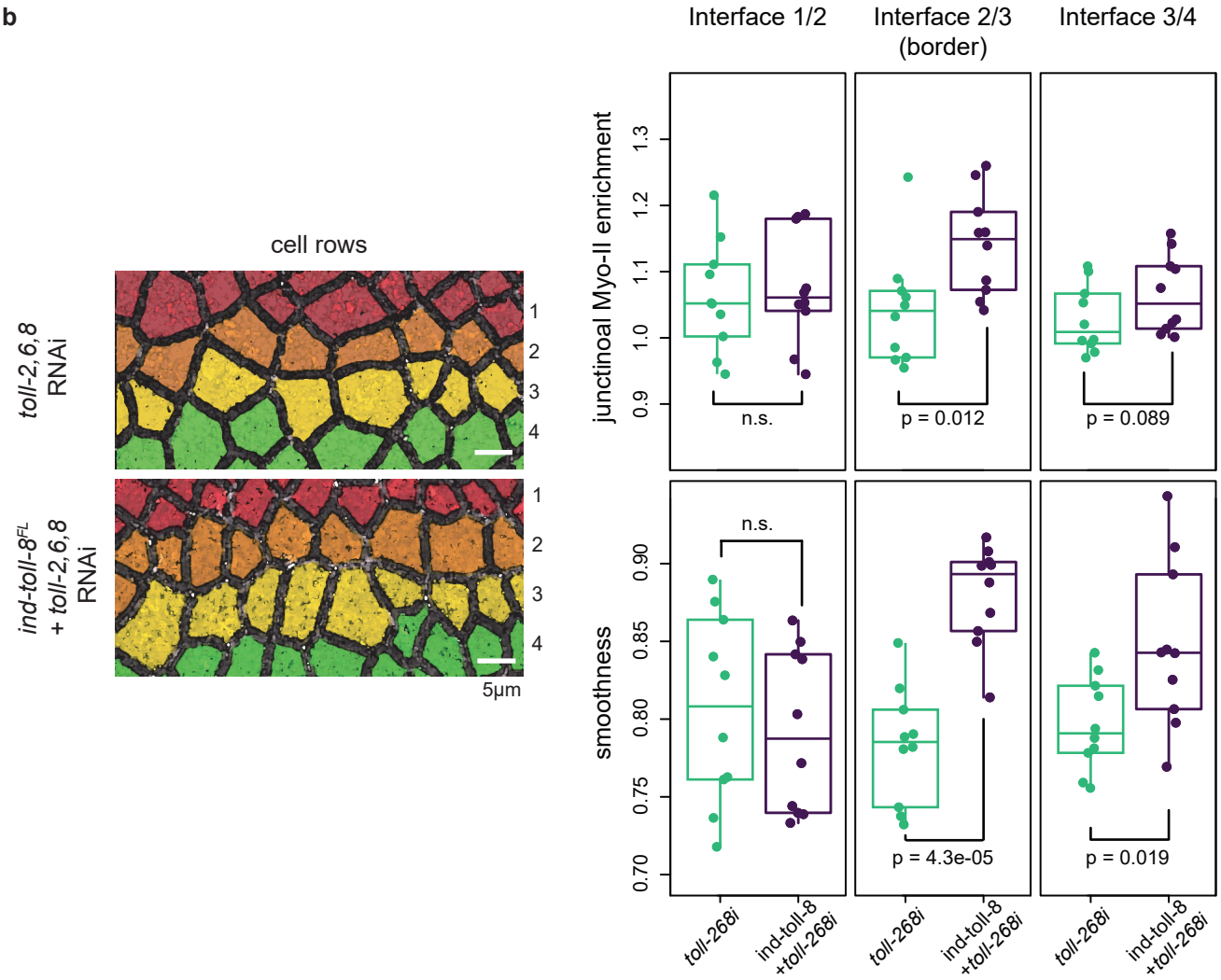

Extended Data Fig. 2 | Quantifications of junctional Myo-II enrichment and boundary smoothness at the *ind* ventral boundary in embryos and at clone borders in wing discs (related to Fig. 1). a, Schematic of the *ind* expression domain (magenta) in an embryo with the ventral boundary (green) of the *ind* domain in zoomed view (left). Schematic of clones (magenta) in wing discs with the clone boundary (green) in zoomed view (right). **b,** Additional quantifications for Fig. 1d. Pseudo colors denote 4 horizontal cell rows in *wt* embryos (top, *n*=10) or embryos expressing ind-Toll-8^{FL}–HA (bottom, *n*-10), both injected with dsRNAs against Toll-2,6,8 (left). Quantifications of junctional Myo-II enrichment (top) and boundary smoothness (bottom) at interfaces 1/2 (left), 2/3 (center) and 3/4 (right). Scalebars: 5 µm. n.s.: $p > 0.05$; Mann-Whitney U test.

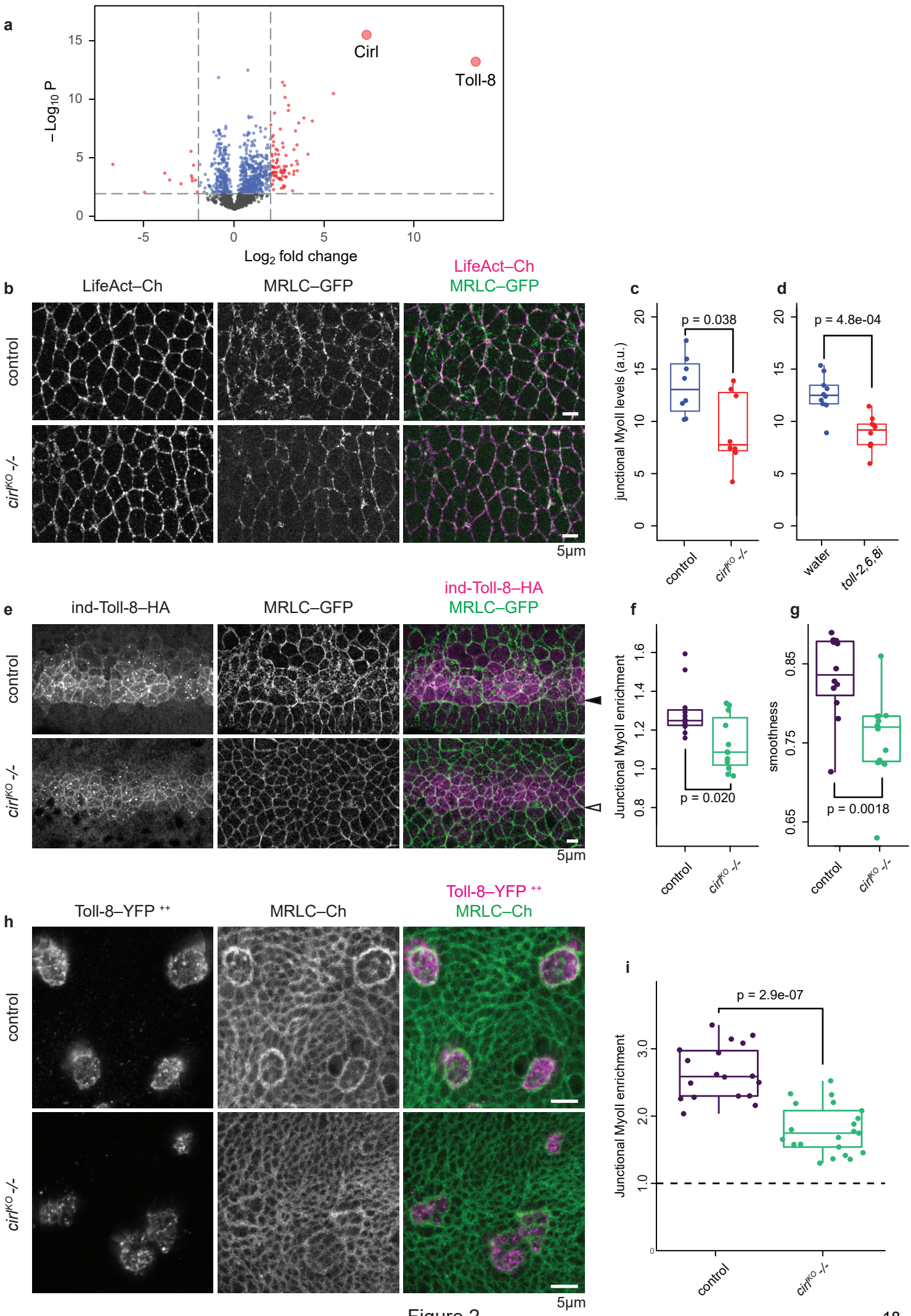
a
Cirl
Toll-8
– Log10 P
Log2 fold change
b
LifeAct–Ch
MRLC–GFP
LifeAct–Ch
MRLC–GFP
control
cirlKO -/-
5µm
c
p = 0.038
junctional MyoII levels (a.u.)
control
cirlKO -/-
d
p = 4.8e-04
water
toll-2,6,8i
e
ind-Toll-8–HA
MRLC–GFP
ind-Toll-8–HA
MRLC–GFP
control
cirlKO -/-
5µm
f
Junctional MyoII enrichment
p = 0.020
control
cirlKO -/-
g
smoothness
p = 0.0018
control
cirlKO -/-
h
Toll-8–YFP ++
MRLC–Ch
Toll-8–YFP ++
MRLC–Ch
control
cirlKO -/-
5µm
i
p = 2.9e-07
Junctional MyoII enrichment
control
cirlKO -/-

Figure 2

Fig. 2 | The GPCR Cirl interacts physically with Toll-8 and is necessary for Myo-II activation induced by Toll-8. a, Volcano plot showing differential levels (Log_2|fold change|, x axis) and p-values ($-Log_{10}$ P, y axis) of proteins identified by mass spectrometry in *Drosophila* embryos overexpressing Toll-8–YFP versus *wt* embryos. Vertical dashed lines denote the cut-off for log2|Fold Change| as 2. Horizontal dashed line denotes the cut-off for p-value as 0.01. **b,** Still images from time lapse movies (left) in *wt* (*n*=8) or *cirl*^{KO} -/- (*n*=8) embryos. LifeAct–Ch marks cell outlines. Junctional Myo-II is reduced in *cirl*^{KO} -/- null mutant embryos. **c,** Quantifications of mean junctional Myo-II levels for the conditions shown in (**b**). **d,** Quantifications of mean junctional Myo-II levels in embryos injected with water (*n*=10) or dsRNAs against Toll-2,6,8 (*n*=10) (related to Extended Data Fig. 2). **e,** Anti-Toll-8–HA (left) and anti-MRLC–GFP (middle) signals in *wt* (top, *n*=12) or *cirl*^{KO} -/- (bottom, *n*=12) embryos expressing full length Toll-8 under the *ind* promoter. Myo-II is reduced at the *ind* ventral boundary in *cirl*^{KO} -/- embryos (empty arrowhead). **f, g,** Junctional Myo-II enrichment (**f**) and boundary smoothness (**g**) are quantified at the ventral *ind* boundary for the conditions shown in (**e**). **h,** Fixed Toll-8–YFP (left) and MRLC–Ch (middle) signals from wing disc clones overexpressing full length Toll-8 in *wt* (top, *n*=18) or *cirl*^{KO} -/- (bottom, *n*=21) wing discs. Myo-II is reduced at the boundary of Toll-8 overexpressing clones in *cirl*^{KO} -/- wing discs. **i,** Junctional Myo-II enrichment is quantified at clone boundaries for the conditions shown in (**h**). Scalebars: 5 µm. n.s.: $p > 0.05$; Mann-Whitney U test.

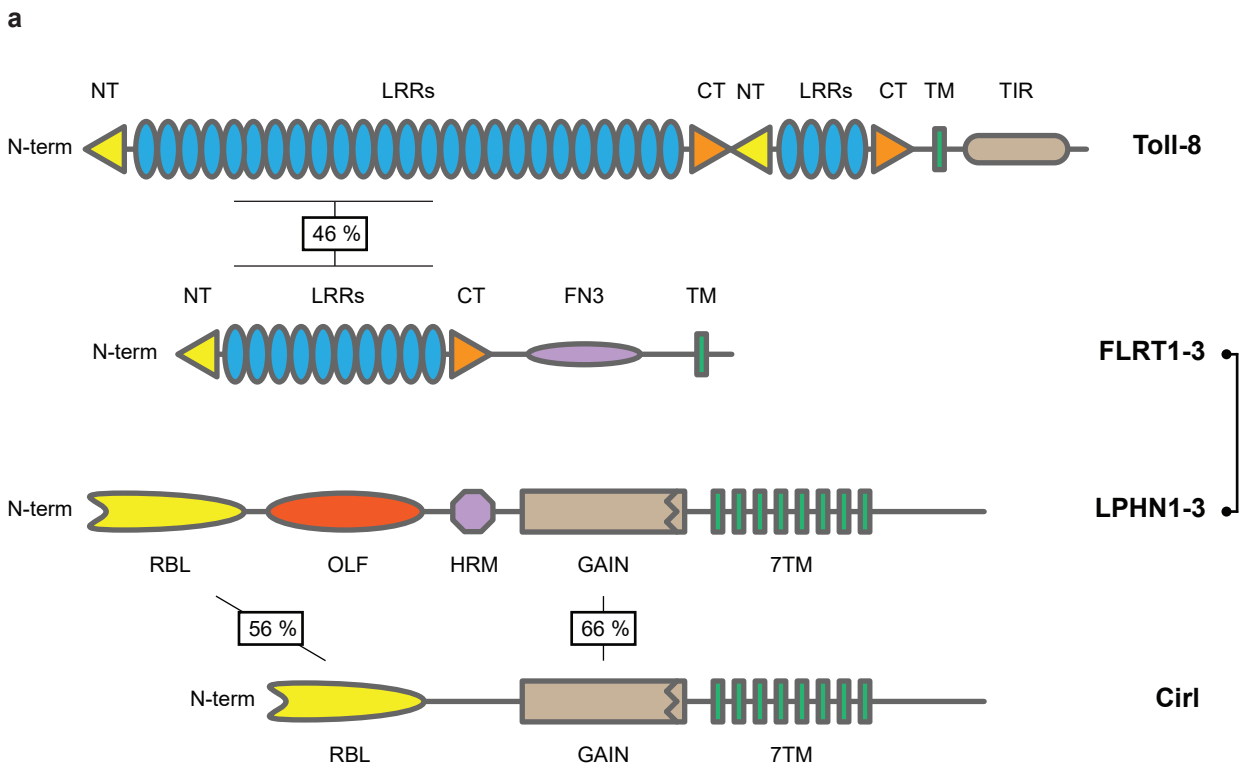

Extended Data Figure 3

Extended Data Fig. 3 | Domain and sequence similarities between *Drosophila* Toll-8/Cirl and human FLRTs/Latrophilins (related to Fig. 2). a, Schematics showing domain assembly for *Drosophila* Toll-8 (top), human FLRT1-3 (upper middle), human Latrophilin/LPHN1-3 (lower middle) and *Drosophila* Cirl (bottom). N-termini are to the left in all schematics. Information on all domains were compiled from literature[20,21] and cross-verified with the Domains and Repeats annotation in Uniprot. Percentages in boxes represent similarities (conservative substitutions) detected in pairwise global alignments of comparable domains using the EMBOSS Needle tool (Needleman-Wunsch algorithm). List of domain abbreviations: 7TM: 7-pass transmembrane domain. CT, Leucine rich repeat C-terminal domain. FN3: Fibronectin 3 domain. GAIN: GPCR autoproteolysis-inducing domain. HRM: Hormone-binding domain. LRRs: Leucine-rich repeats. NT, Leucine rich repeat N-terminal domain. OLF: Olfactomedin domain. RBL: Rhamnose-binding lectin domain. TIR: Toll/Il-1 Receptor domain. TM: Transmembrane domain.

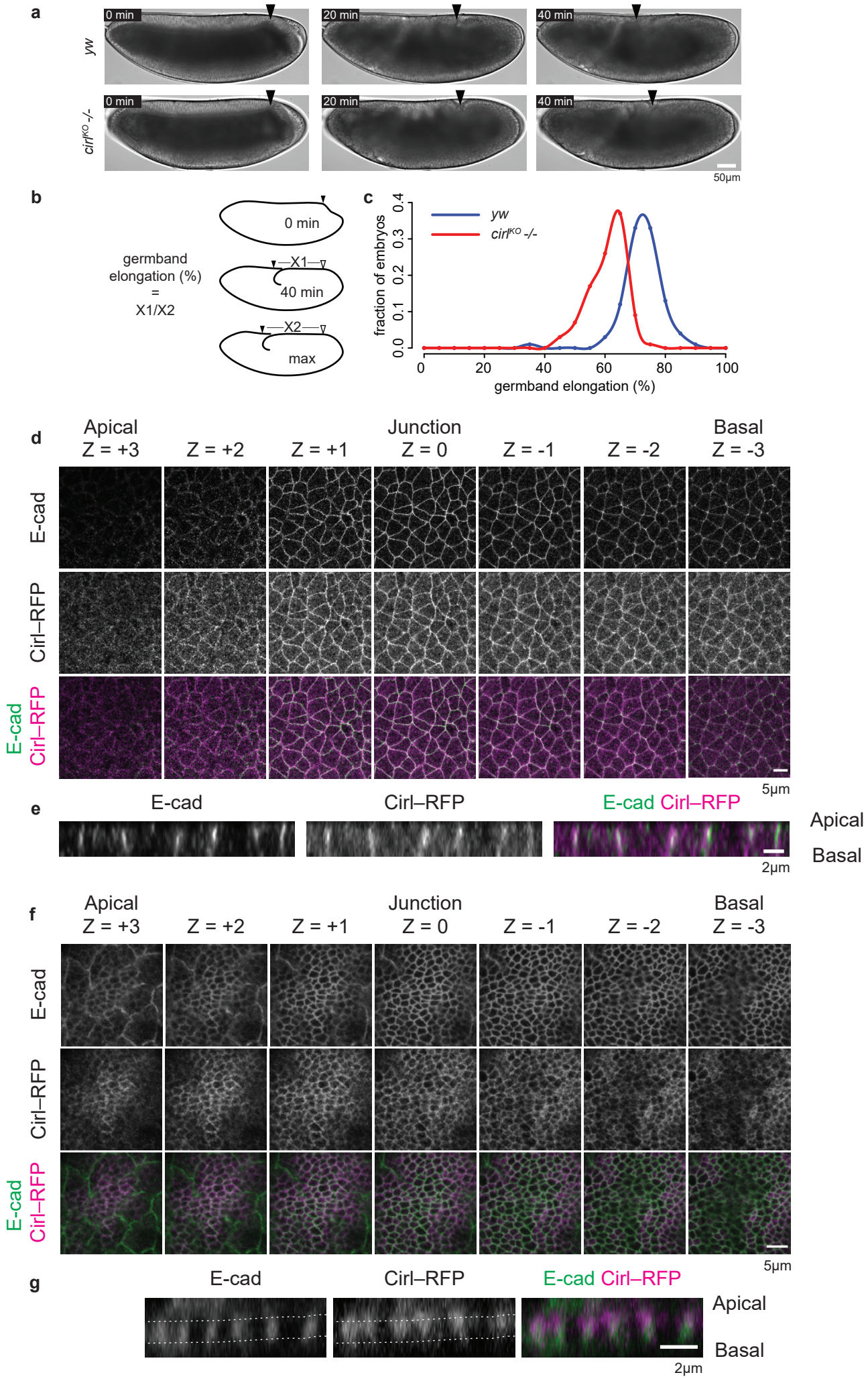

Extended Data Figure 4

Extended Data Fig. 4 | Cirl protein is enriched at adherens junctions and in the subapical domain in *Drosophila* embryonic germband and wing discs cells (related to Fig. 2). a, Axial extension at 0, 20 and 40 minutes in *yw* (top) and *cirl*^{KO} -/- (bottom) embryos. 0 min is defined as the beginning of axial extension. Arrowheads denote the dorsal edge of the posterior midgut primordium. Axial extension is slowed down in the absence of *cirl*. **b,** Schematics showing quantifications of axial extension as a ratio of posterior midgut primordium migration distance at 40 minutes (x1) over its maximum migration distance (x2). **c,** Histogram of axial extension for *yw* (blue, n=100) and *cirl*^{KO} -/- (red, n=89) embryos. **d,** Anti E-cad (green) and anti Cirl–RFP (magenta) signals in the ectoderm epithelium in stage 7 *Drosophila* embryos. Sequential Z planes are shown from apical (left) to basal (right). Step size: 0.38 µm. **e,** Orthogonal views of the condition shown in (**d**), apical to the top, basal to the bottom. **f,** Anti E-cad (green) and anti Cirl–RFP (magenta) signals in the wing disc pouch epithelium. Sequential Z planes are shown from apical (left) to basal (right). Step size: 0.25 µm. **g,** Orthogonal views of the condition shown in (**f**), apical to the top, basal to the bottom. Dotted lines indicate the junctional plane, Cirl–RFP is localized at adherens junctions and in the subapical domain above junctions. Scalebars: 5 µm in (**d**) and (**f**); 2 µm in (**e**) and (**g**).

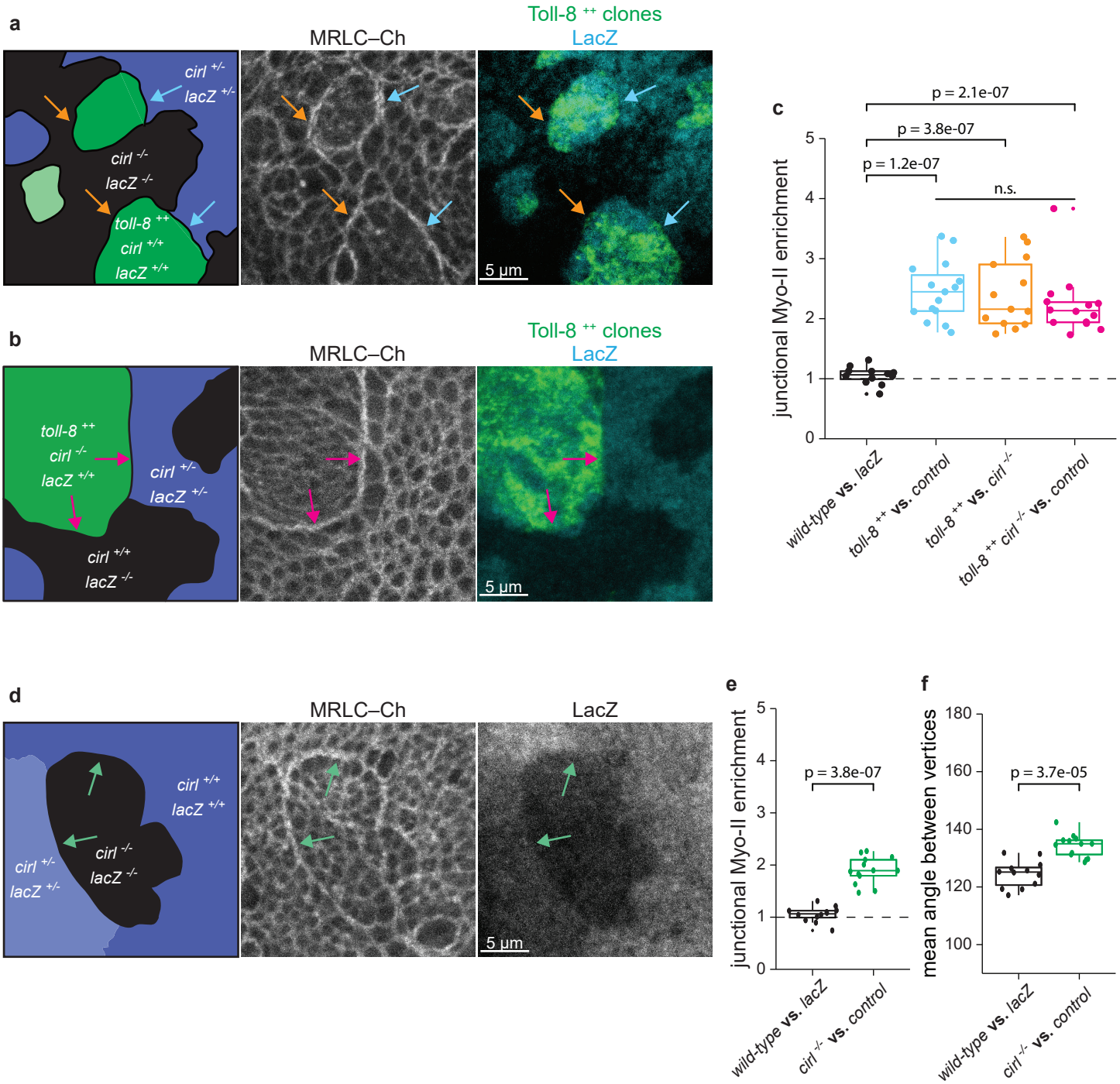
a
MRLC–Ch
Toll-8 ++ clones
LacZ
cirl +/-
lacZ +/-
cirl -/-
lacZ -/-
toll-8 ++
cirl +/+
lacZ +/+
5 µm
b
MRLC–Ch
Toll-8 ++ clones
LacZ
toll-8 ++
cirl -/-
lacZ +/+
cirl +/-
lacZ +/-
cirl +/+
lacZ -/-
5 µm
c
p = 2.1e-07
p = 3.8e-07
p = 1.2e-07
n.s.
junctional Myo-II enrichment
0
1
2
3
4
5
wild-type vs. lacZ
toll-8 ++ vs. control
toll-8 ++ vs. cirl -/-
toll-8 ++ cirl -/- vs. control
d
MRLC–Ch
LacZ
cirl +/+
lacZ +/+
cirl -/-
lacZ -/-
cirl +/-
lacZ +/-
5 µm
e
junctional Myo-II enrichment
p = 3.8e-07
0
1
2
3
4
5
wild-type vs. lacZ
cirl -/- vs. control
f
mean angle between vertices
p = 3.7e-05
100
120
140
160
180
wild-type vs. lacZ
cirl -/- vs. control

Figure 3

Fig. 3 | Cirl asymmetric expression activates Myo-II. a, MARCM clones in a wing disc where clones overexpressing Toll-8–YFP (*toll-8* $^{++}$ in green) are juxtaposed to control cells heterozygous (*cirl* $^{+/-}$ in blue, cyan arrows, *n*=15) or null mutant (*cirl* $^{-/-}$ in black, orange arrows, *n*=13) for *cirl*. Myo-II activation at the boundary of Toll-8 overexpressing cells is similar in both cases. **b,** MARCM clones in the wing disc. Myo-II is activated at boundaries (magenta arrows, *n*=14) of clones overexpressing Toll-8–YFP and null mutant for *cirl* (*toll-8* $^{++}$, *cirl* $^{-/-}$ in green) juxtaposed to cells heterozygous (*cirl* $^{+/-}$ in blue) or *wild-type* (*cirl* $^{+/+}$ in black) for *cirl*. **c,** Quantifications of junctional Myo-II enrichment at clone boundaries for the conditions shown in (**a**) and (**b**). With the exception of control clones (black boxplot, images not shown, *n*=12), colors of the boxplots correspond to the arrows in (**a**) and (**b**). **d,** Myo-II is activated at the boundary (green arrows) of *cirl*$^{-/-}$ null mutant clones (*cirl*$^{-/-}$ in black, *n*=13) in the wing disc. **e, f,** Junctional Myo-II enrichment (**e**) and boundary smoothness (**f**) quantified at clone boundaries for the conditions shown in (**d**). The black plot (images not shown) in (**e**) is the same as in (**c**). Scalebars: 5 µm. n.s.: $p > 0.05$; Mann-Whitney U test.

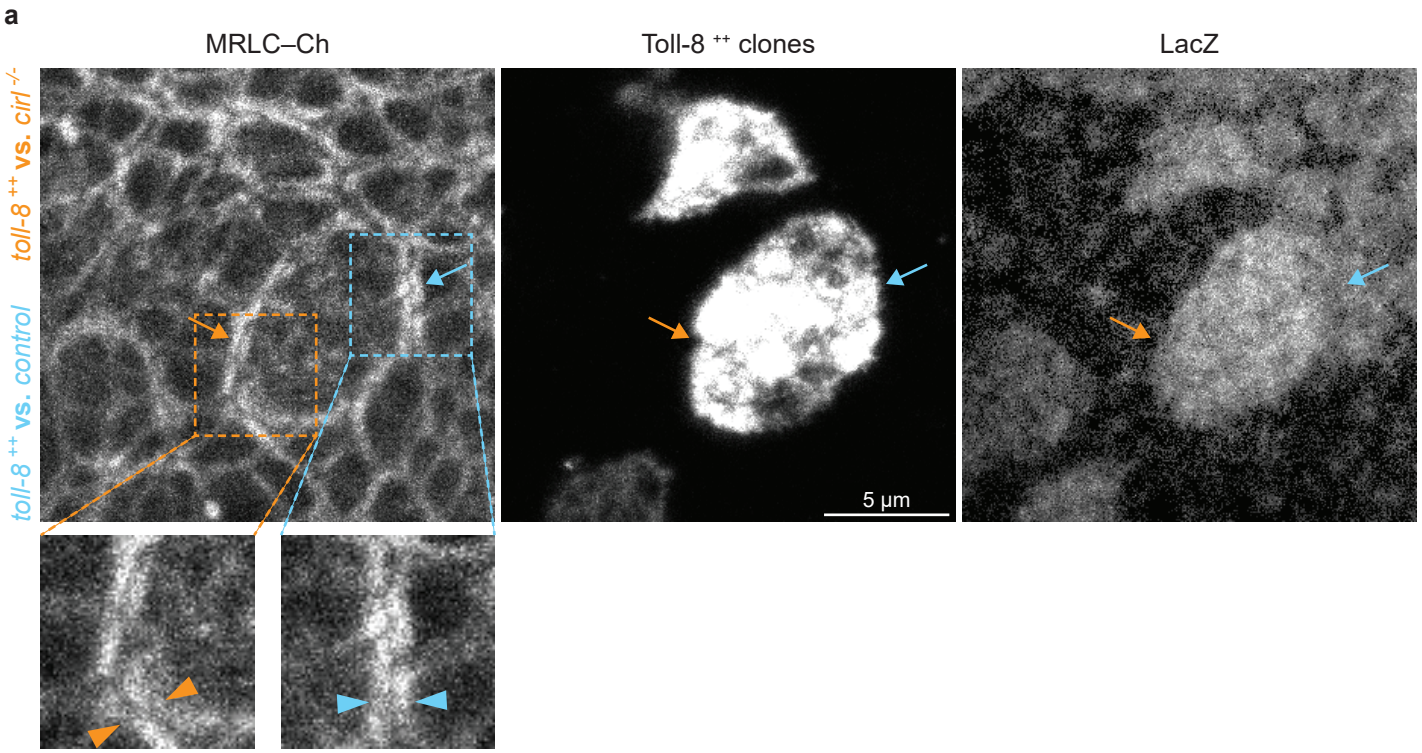

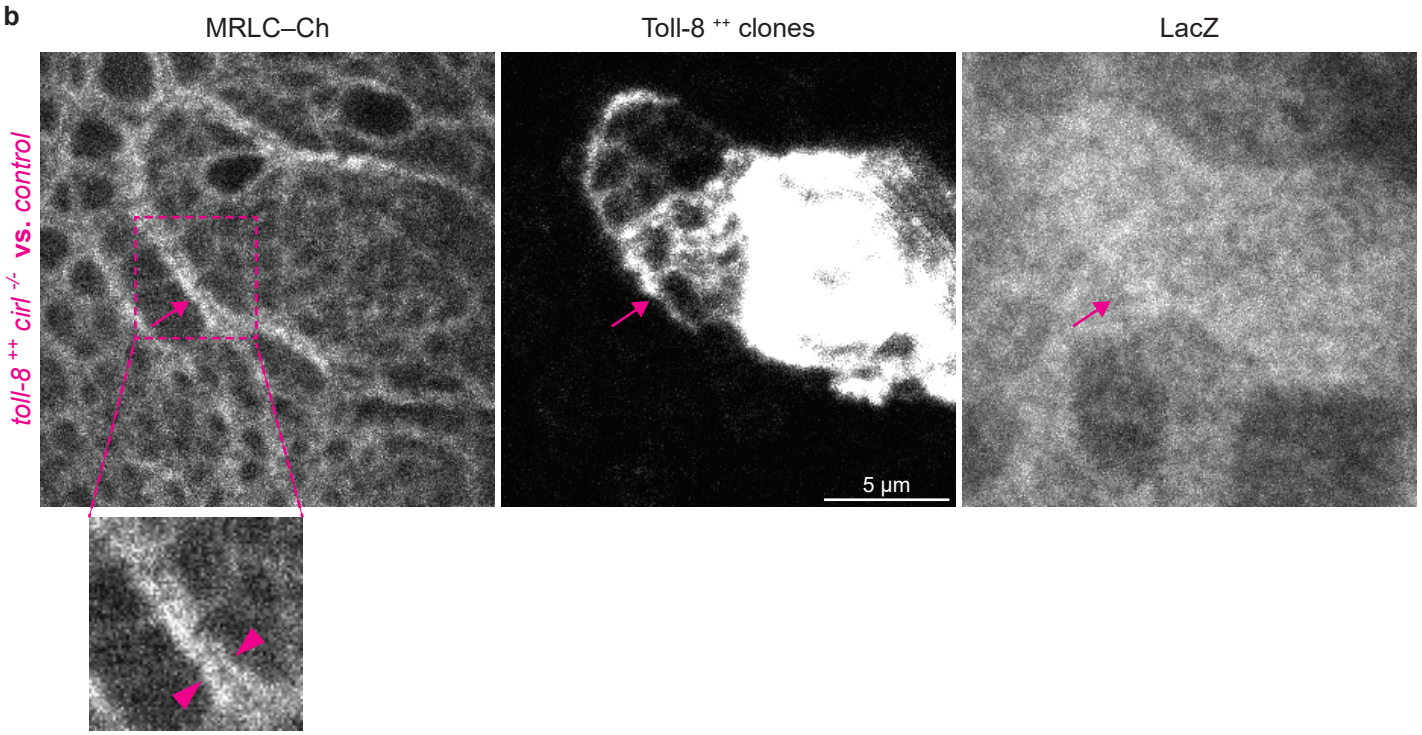

Extended Data Figure 5

Extended Data Fig. 5 | Myo-II is activated on both sides of the Toll-8 expression boundary (related to Fig. 3). a, Myo-II activation in MARCM clones in the wing disc where cells overexpressing Toll-8–YFP (*toll-8* $^{++}$, *lacZ* $^{+/+}$, green in Fig. 3a) are juxtaposed with control cells heterozygous (*cirl* $^{+/-}$, *lacZ* $^{+/-}$, blue in Fig. 3a, cyan arrow) or null mutant (*cirl* $^{-/-}$, *lacZ* $^{-/-}$, black in Fig. 3a, orange arrow) for *cirl*. The cyan and orange arrowheads on the zoomed images indicate Myo-II activation on both sides of clone boundaries (related to Fig. 3a). **b,** MARCM clones in the wing disc. Myo-II is activated at clone boundaries (magenta arrow) where cells overexpressing Toll-8–YFP and null mutant for *cirl* (*toll-8* $^{++}$, *cirl* $^{-/-}$, *lacZ* $^{+/+}$, green in Fig. 3b) are juxtaposed with cells heterozygous (*cirl* $^{+/-}$, *lacZ* $^{+/-}$ in blue in Fig. 3b) or *wild-type* (*cirl* $^{+/+}$, *lacZ* $^{-/-}$ in black in Fig. 3b) for *cirl*. The magenta arrowheads on the zoomed image mark Myo-II activation on both sides of the clone boundary (related to Fig. 3b). Scalebars: 5 µm.

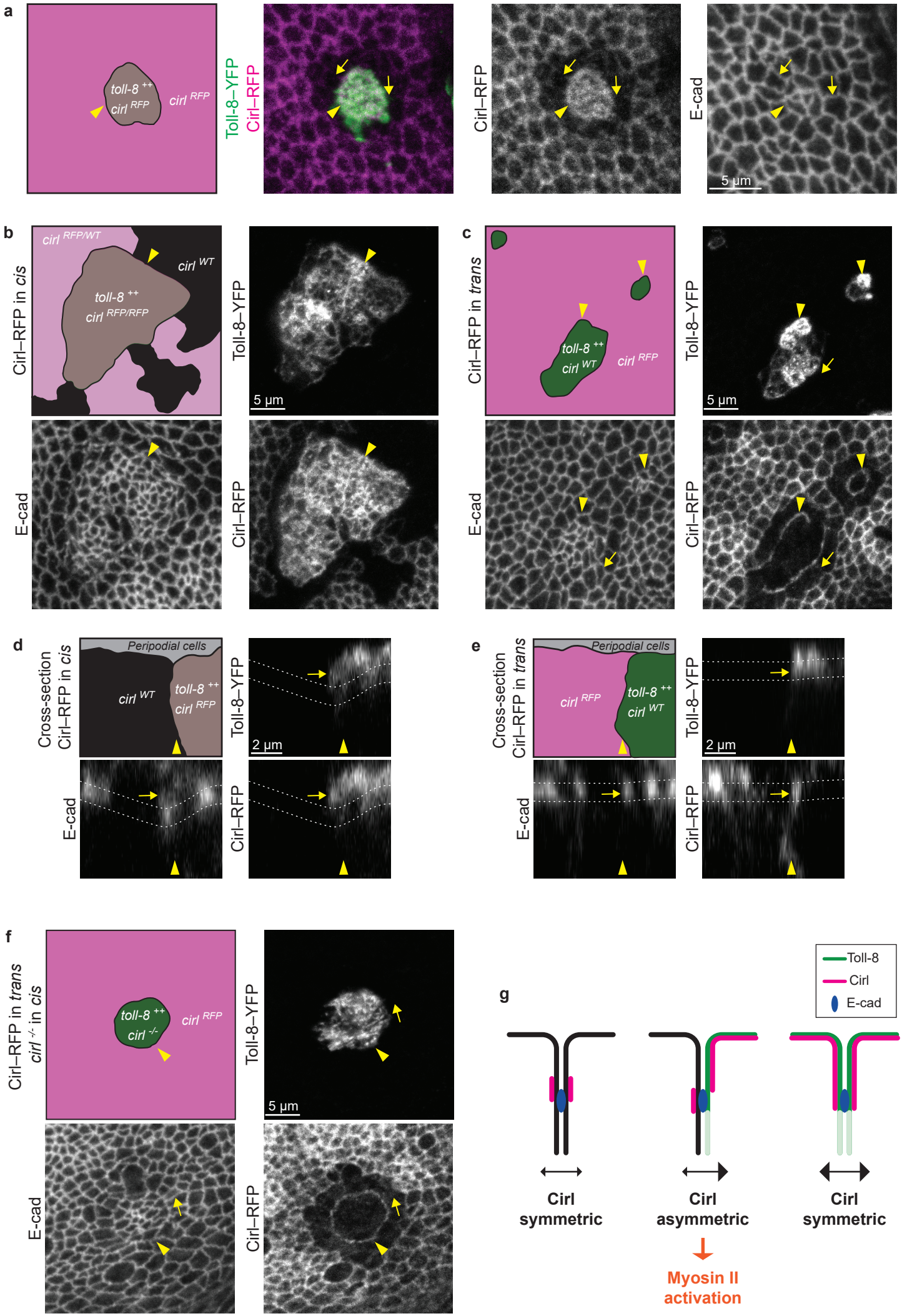
a
toll-8 ++
cirl RFP
cirl RFP
Toll-8–YFP
Cirl–RFP
Cirl–RFP
E-cad
5 µm
b
Cirl–RFP in cis
cirl RFP/WT
cirl WT
toll-8 ++
cirl RFP/RFP
Toll-8–YFP
5 µm
E-cad
Cirl–RFP
c
Cirl–RFP in trans
toll-8 ++
cirl WT
cirl RFP
Toll-8–YFP
5 µm
E-cad
Cirl–RFP
d
Cross-section
Cirl–RFP in cis
Peripodial cells
cirl WT
toll-8 ++
cirl RFP
Toll-8–YFP
2 µm
E-cad
Cirl–RFP
e
Cross-section
Cirl–RFP in trans
Peripodial cells
cirl RFP
toll-8 ++
cirl WT
Toll-8–YFP
2 µm
E-cad
Cirl–RFP
f
Cirl–RFP in trans
cirl -/- in cis
toll-8 ++
cirl -/-
cirl RFP
Toll-8–YFP
5 µm
E-cad
Cirl–RFP
g
Toll-8
Cirl
E-cad
Cirl
symmetric
Cirl
asymmetric
Cirl
symmetric
Myosin II
activation

Figure 4

Fig. 4. | Toll-8 generates Cirl interfacial asymmetry at the boundary of its expression domain. Arrowheads indicate clone boundaries in all panels. **a,** Toll-8–YFP overexpressing clone (*toll-8* $^{++}$, *cirl* ^{RFP} in brown) in a Cirl–RFP wing disc. Toll-8–YFP (green) and anti Cirl–RFP (magenta) signals colocalize inside the clone (central left). Cirl–RFP is depleted from junctions orthogonal to the clone boundary (arrows). **b,** Toll-8–YFP overexpressing clone with Cirl–RFP present inside (*toll-8* $^{++}$, *cirl* ^{RFP} in brown) facing cells homozygous for untagged Cirl (*cirl* ^{WT} in black) or heterozygous for *cirl* ^{RFP} (*cirl* $^{RFP/WT}$ in light magenta). **c,** Toll-8–YFP overexpressing clones (*toll-8* $^{++}$, *cirl* ^{WT} in green) in a wing disc where Cirl–RFP is present only outside of Toll-8 overexpressing clones (*cirl* ^{RFP} in magenta). The variation in Cirl–RFP levels is due to that cells can be homozygous or heterozygous for *cirl* ^{RFP}. Cirl–RFP is depleted from junctions orthogonal to the clone boundary (arrow) and accumulate at the clone boundary (arrowheads). **d, e,** Orthogonal views of the conditions shown in (**b**) and (**c**), respectively (apical to the top). Dotted lines indicate the junctional plane. Arrows mark Cirl–RFP enrichment at the junctional plane (**e**, *in trans*) or above the junctional plane (**d**, *in cis*). **f,** Same experiment as in (**c**), except that *cirl* is null mutant instead of untagged in Toll-8 overexpressing clones (*toll-8* $^{++}$, *cirl* $^{-/-}$ in green). **g,** Model proposing Myo-II activation due to Cirl asymmetric localization induced at Toll-8 expression borders. Scalebars: 5 µm in (**a-c**) and (**f**); 2 µm in (**d**) and (**e**).

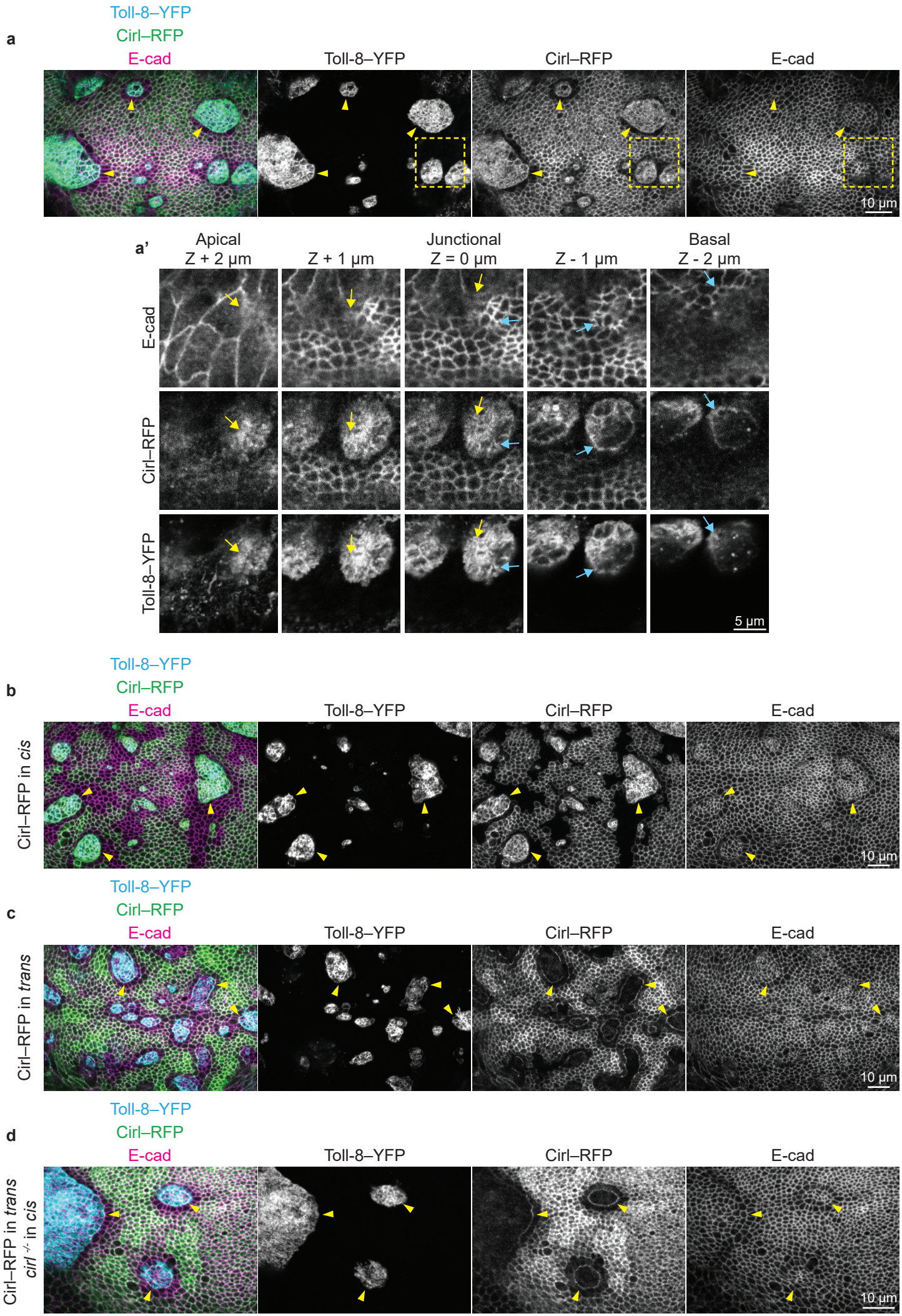

Extended Data Figure 6

Extended Data Fig. 6 | Large scale views of the effect of Toll-8 overexpression on Cirl distribution in the wing disc (related to Fig. 4). Arrowheads indicate clone boundaries in all panels. **a,** Toll-8–YFP overexpressing clones in a Cirl–RFP wing disc (related to Fig. 4a). **a',** Sequential Z planes are shown from apical (left) to basal (right) for the region highlighted in (**a**). Arrows indicate colocalization between Toll-8–YFP and Cirl–RFP at the apical plane (yellow arrows) and at the junctional plane defined by E-cad (cyan arrows). **b,** Toll-8–YFP overexpressing clones with Cirl–RFP present inside facing cells homozygous for untagged Cirl or heterozygous for *cirl* ^{RFP} (related to Fig. 4b). **c,** Toll-8–YFP overexpressing clones in a wing disc where Cirl–RFP is present only outside of Toll-8 overexpressing clones (related to Fig. 4c). Variation in Cirl–RFP levels is due to that cells can be homozygous or heterozygous for *cirl* ^{RFP}. **d,** Same experiment as in (**c**), except that *cirl* is mutant instead of being untagged in Toll-8 overexpressing clones (related to Fig. 4f). Scalebars: 10 µm in (**a**) and (**b-d**); 5 µm in (**a'**).

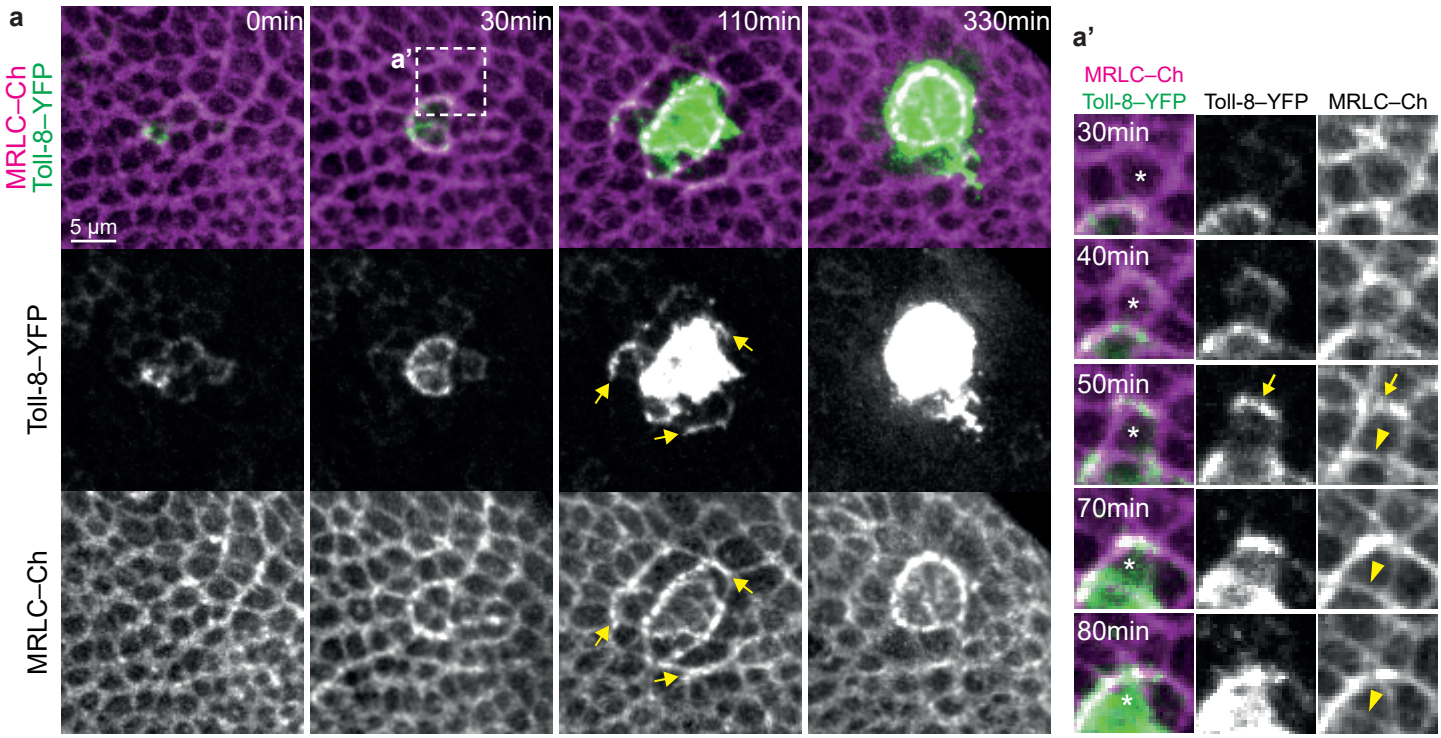
a
MRLC–Ch
Toll-8–YFP
0min
30min
110min
330min
a'
5 µm
Toll-8–YFP
MRLC–Ch
a'
MRLC–Ch
Toll-8–YFP
Toll-8–YFP
MRLC–Ch
30min
40min
50min
70min
80min

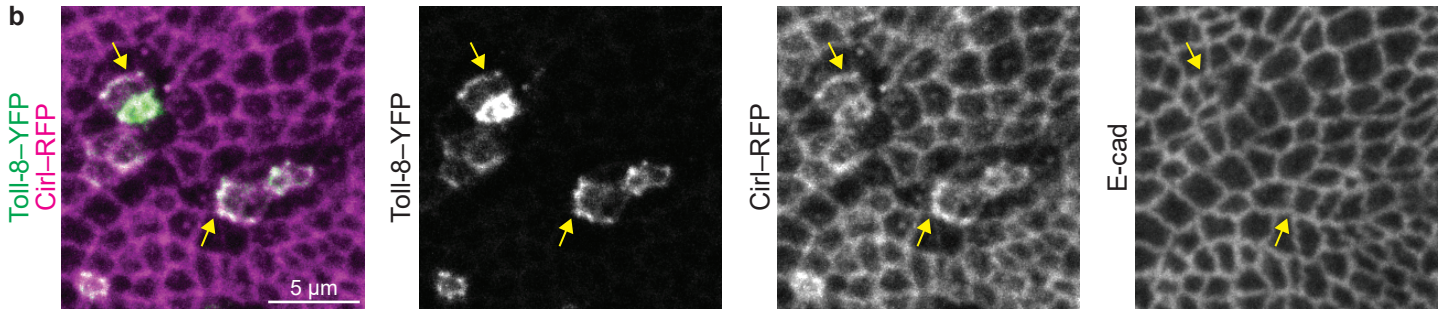
b
Toll-8–YFP
Cirl–RFP
5 µm
Toll-8–YFP
Cirl–RFP
E-cad

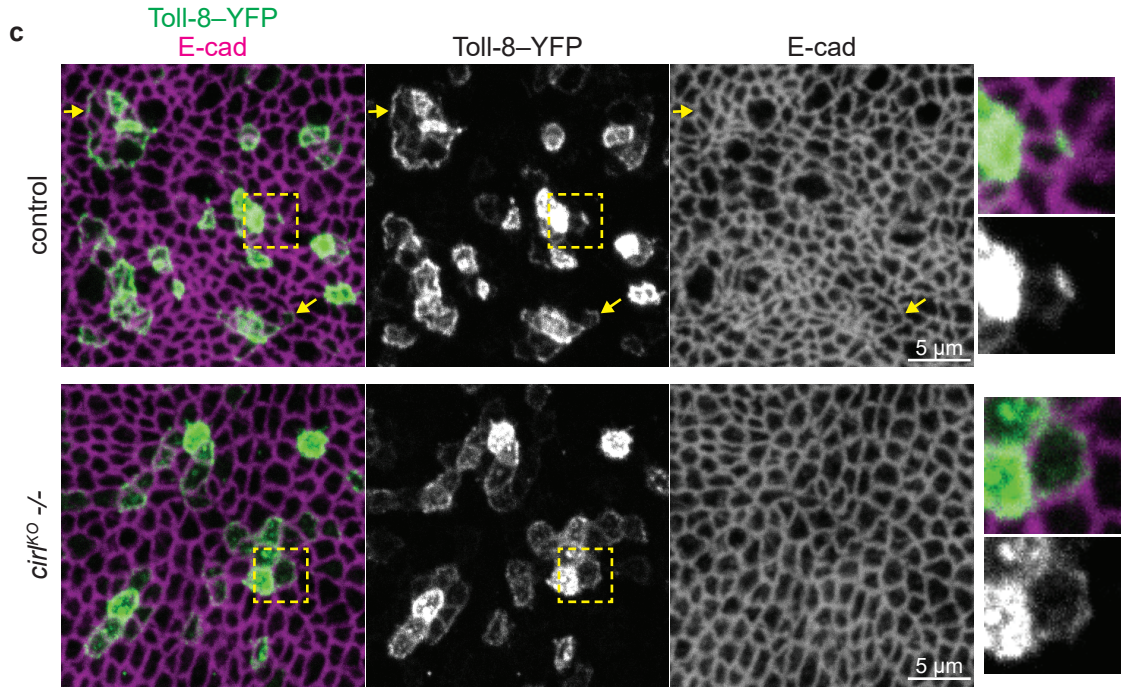
c
Toll-8–YFP
E-cad
Toll-8–YFP
E-cad
control
cirl^KO -/-
5 µm
5 µm

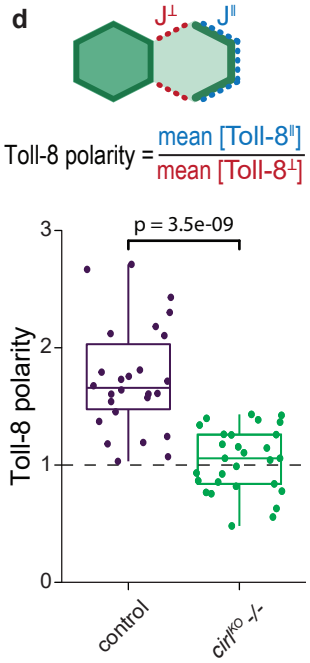
d
J⊥
J∥
Toll-8 polarity = mean [Toll-8∥] / mean [Toll-8⊥]
p = 3.5e-09
Toll-8 polarity
3
2
1
0
control
cirl^KO -/-

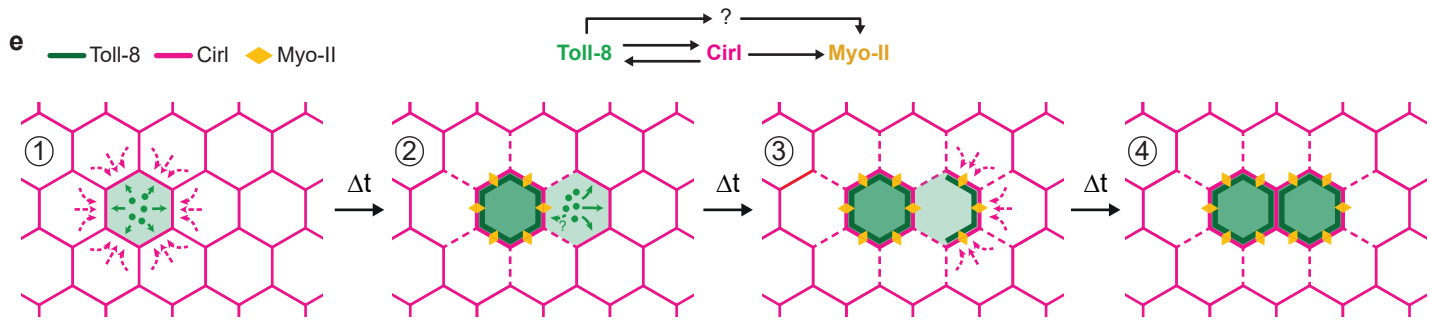
e
Toll-8
Cirl
Myo-II
?
Toll-8
Cirl
Myo-II
①
②
③
④
Δt
Δt
Δt

Figure 5

Fig. 5 | Toll-8 and Cirl form dynamic self-organized patterns. a, Stills from a time lapse movie of a wing disc showing live dynamics of Toll-8–YFP (green) and MRLC–Ch (magenta) in a nascent Toll-8–YFP overexpressing clone. Toll-8–YFP starts being detectable at 0 min and its levels increase during the course of the time lapse. Arrows mark junctions displaying Toll-8 planar polarized enrichment resulting in Myo-II activation. **a',** Zoomed view of a cell that dynamically upregulates expression of Toll-8–YFP during ~50min (asterisk). Myo-II is being activated at junctions that show Toll-8–YFP planar polarity (arrow) and being deactivated once Toll-8–YFP expression reaches similar levels between contacting cells (arrowhead). **b,** Nascent Toll-8–YFP clones (green) in a Cirl–RFP (magenta) wing disc. Cirl levels are increased at Toll-8–YFP enriched junctions (arrows). **c,** Toll-8–YFP planar polarity in nascent Toll-8–YFP clones in control (top, *n*=26) or *cirl* null mutant (bottom, *n*=29) wing discs. Zoomed views are shown on the right. Toll-8–YFP planar polarity is reduced in the absence of Cirl. **d,** Quantifications of Toll-8–YFP planar polarity in cells expressing low Toll-8–YFP levels in direct contact with cells expressing high Toll-8–YFP levels for the conditions shown in (**c**). **e,** Model proposing mutual attraction between Toll-8 and Cirl leading to the formation of self-organized planar polarized patterns of Toll-8/Cirl/Myo-II (refer to the main text for a detailed description). Scalebars: 5 µm.

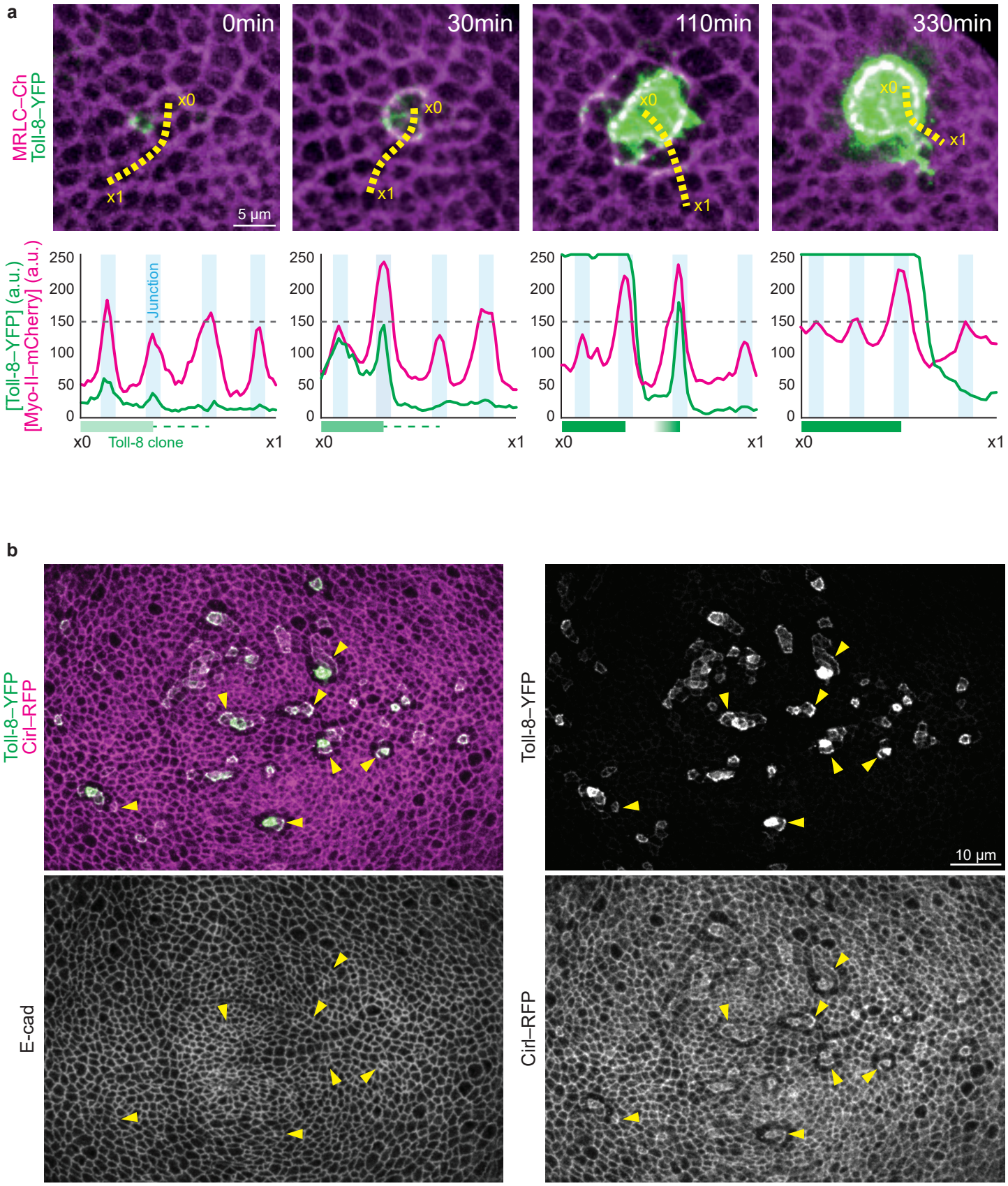

Extended Data Figure 7

Extended Data Fig. 7 | Additional quantifications and large scale view of nascent Toll-8 overexpressing clones (related to Fig. 5). a, Quantifications of temporal dynamics of Toll-8–YFP (green) and MRLC–Ch (magenta) at the boundary of a nascent Toll-8–YFP overexpressing clone in the wing disc (panels taken from Fig. 5a). Toll-8-YFP and MRLC-Ch levels were quantified along a line (yellow, from x0 to x1) at representative stages of clonal Toll-8 upregulation. Myo-II is activated at the boundary of Toll-8–YFP expressing cells facing Toll-8–YFP negative cells (middle left). Myo-II is also activated at interfaces between cells expressing different levels of Toll-8–YFP (middle right) leading to multiple rows of Myo-II activation. Once Toll-8–YFP levels equalize between cells, Myo-II only remains activated at junctions that display differences in Toll-8 expression (right). **b,** Large scale view of nascent Toll-8–YFP clones (green) in a Cirl–RFP (magenta) wing disc (related to Fig. 5b). Cirl–RFP is attracted to Toll-8–YFP enriched junctions (see arrowheads). Scalebars: 5 µm in (**a**) and 10 µm in (**b**).

Movie Legends

Supplementary Video 1: Time lapse movie of a wing disc showing live dynamics of Toll-8–YFP (green) and MRLC–Ch (magenta) in a nascent Toll-8–YFP overexpressing clone. Toll-8–YFP starts being detectable at 0 min and its levels increase during the course of the time lapse. Asterisks indicate a cell that dynamically upregulates expression of Toll-8–YFP during ~50min. Myo-II is being activated at junctions that show Toll-8–YFP planar polarity (arrow) and being deactivated once Toll-8–YFP expression reaches similar levels between contacting cells (arrowheads). Scalebar: 5 μm.

Supplementary Video 2: Time lapse movie of a wing disc showing live dynamics of Toll-8–YFP (green) and MRLC–Ch (magenta) in a nascent Toll-8–YFP overexpressing clone. Scalebar: 5 μm.

Supplementary Video 3: Time lapse movie of a wing disc showing live dynamics of Toll-8–YFP (green) and MRLC–Ch (magenta) in Toll-8–YFP overexpressing clones. Scalebar: 5 μm.

Supplementary Table Legends

Supplementary Table 1: List of proteins associated with Toll-8 (in green) selected using pFDR at 0.1% and s0=1. The proteomes of embryos overexpressing Toll-8–YFP maternally and zygotically (N = 3 protein isolations: T3, T4, T5, each with 3 replicas: T3a, T3b, T3c, …) were compared with yw embryos (N = 3 protein isolations: C3, C4, C5, each with 3 replicas: C3a, C3b, C3c, …) with affinity purification mass spectrometry (PRIDE dataset identifier PXD017895). Protein list is displayed by order of Difference log2(T/C). Rows highlighted in green denote significant hits from a two-sample t-test using permutation-based false discovery rate (pFDR) controlled at 0.1% (5000 permutations).

Supplementary Table 2: List of genotypes employed in the experiments in the indicated figure panels.

Methods

Fly strains and genetics

The following mutant alleles and insertions were used: *ind-Toll-8^{FL}::HA* (attP40 on 2L), *ind-Toll-8$^{\Delta LRR}$::HA* (attP40 on 2L), *UASp-Toll-8^{FL}::eGFP* (attP40 on 2L), *UASp-Toll-8$^{\Delta LRR}$::eGFP* (attP40 on 2L), *UASp-Toll-8$^{\Delta Cyto}$::eGFP* (attP40 on 2L), *UASt-Toll-8::sYFP2* (attP9744 on 3R), *Cirl^{KO}* (LAT84 and LAT154, gifts from T. Langenhan)[19], *Cirl::RFP* knock-in[26] (*Cirl::RFP^{KIN}*, LAT159, gift from T. Langenhan), *sqh-Lifeact::mCherry* (attP9744 on 3R, gift from P.F. Lenne), *E-cad::eGFP* knock-in[38] (*E-cad::eGFP^{KIN}*), *eve::sYFP2^{BAC}* (BAC construct, S2E.MSE.eve.YFP, FBal0279504, gift from M. Ludwig)[39], *hs-FLP*[40], *Act5C>STOP>GAL4* (Bloomington BL 4780), *FRT42D* (Bloomington BL 1802), *FRT42D arm-LacZ* (Bloomington BL 7372), *FRT42D tub-GAL80* (Bloomington BL 9917), *tub-GAL80ts* (Bloomington BL 7108) and *tub-GAL80ts* (Bloomington BL 7017). *67-Gal4* ({matαtub-GAL4-VP16}67) is a ubiquitous, maternally supplied GAL4 driver (gift from E. Wieschaus). MRLC is encoded by the gene *spaghetti squash* (*sqh*, Genebank ID: AY122159). Sqh was visualized using *sqh-Sqh::mCherry* (attP9736 on 2R or attP9744 on 3R for experiments in the wing disc or a construct on chromosome 2 from A. Martin[41] for live-imaging experiments in the embryo) and *sqh-Sqh::eGFP* transgenics (gift from R. Karess).

All fly constructs and genetics are listed in Supplementary Table 2.

Constructs and transgenesis

<u>*Expression vectors drivers:*</u> UASp expression vector driver was generated by inserting a PhiC31 attB sequence downstream from the K10 3'-UTR of pUASp. UASt expression vector driver corresponds to pUASTattB which contains a PhiC31 attB sequence inserted downstream from the SV40 3'-UTR[42].

ind is an early horizontal stripe expression vector driver generated by modifying the *pbphi-evePr-MS2-yellow*[43] (gift from T. Gregor) as follows. First, EVEstr2 enhancer sequence was replaced by the ind$^{1.4}$ enhancer[44] (gift from Gerardo Jiménez). Second, a part of Hsp70Bb 5'-UTR was added after the eve basal promoter. Third, MS2-yellow sequence was replaced by a small polylinker for further cloning.

<u>*Expression vectors constructs and transgenics:*</u> *Toll-8* (*Tollo*, CG6890) whole ORF was amplified using a pACMAN genomic plasmid and cloned inside each expression vector. *UASp-Toll-8^{FL}::eGFP* is a Cter mEGFP tag construct of full length Toll-8 (1346aa) with a GSAGSAAGSGEF flexible aa linker in between. *UASp-Toll-8$^{\Delta Cyto}$::eGFP* is a cytoplasmic truncated version of this vector (deletion from aa H1052 to M1346 last aa). In *UASp-Toll-8$^{\Delta LRR}$::eGFP*, all LRR repeats were removed (deletion from aa E99 to L917). *UASt-Toll-8::sYFP2* is a Cter sYFP2 tag construct of full length Toll-8 with a GSAGSAAGSGEF flexible aa linker in between. *ind-Toll-8^{FL}::HA* is a Cter HA tag construct of full length Toll-8 with no linker in between. In *ind-Toll-8$^{\Delta LRR}$::HA*, all LRR repeats were removed (deletion from aa E99 to L917).

All recombinant expression vectors were built using "In-Fusion cloning" (Takara Bio), verified by sequencing (Genewiz) and sent to BestGene Incorporate for PhiC31 site specific mediated transgenesis into attP40 (2L, 25C7) or 9744 (3R, 89E11). Fully annotated FASTA sequences of all these vectors are available on request.

Antibodies

The following primary antibodies were used: rat-anti-E-Cad (1:200, DHSB DCAD2 concentrate), mouse-anti-β-catenin (1:400, DHSB N2 7A1 Armadillo concentrate), mouse-anti-LacZ (1:100, DHSB 40-1a concentrate), rat-anti-HA (1:100, Anti-HA High Affinity rat IgG_1, Roche ROAHAHA). Sqh::eGFP was detected with rabbit-anti-GFP (1:500, Life Technologies A11122 or 1:1000 Abcam ab6556). Cirl::RFP was detected with rabbit-anti-RFP (1:1000, Rockland 600-401-679). The following secondary antibodies were used: donkey-anti-rabbit Alexa Fluor 488 IgG (Life Technologies A 21206), donkey-anti-rabbit Alexa Fluor 568 IgG (Life Technologies A10042), donkey anti-mouse Alexa Fluor 568 IgG (Life Technologies A10037), donkey-anti-mouse Alexa Fluor 647 IgG (Jackson ImmunoResearch 715 605 151) and donkey-anti-rat Alexa Fluor 647 IgG (Jackson ImmunoResearch 712 605 153). All secondary antibodies were used at 1:500.

Affinity Purification Mass Spectrometry

Protein purification and mass spectrometry: Roughly 600 embryos for each sample were collected from overnight cages kept at 25°C for the following crosses: *yw* (control) or females *; 67-GAL4/+; UASt-Toll-8::sYFP2/+;* x males *; 67-GAL4/+; UASt-Toll-8::sYFP2/+;* (Toll-8::YFP maternal and zygotic overexpression), dechorionated with bleach, transferred directly to lysate buffer (10 mM Tris/Cl pH 7.5; 150 mM NaCl; 0.5 mM EDTA; 0.5% NP-40, supplemented with protease and phosphatase inhibitors) and crushed manually on ice over 30 minutes. Lysates were centrifuged to clear debris and protein concentrations of post-centrifugation supernatants were determined. The crude protein yield per lysate sample is usually 1000~3000 µg. In each experiment, lysates of comparable protein concentration were incubated with pre-rinsed GFP nano-trap agarose resin (Chromotek, gta-20) at 4°C for 90 min, rinsed 3 x and resuspended in 2x Laemmli buffer with DTT. Protein extraction and purification was performed 3 times each for each cross and verified with silver staining. Protein samples were further purified on NuPAGE 4-12% Bis-Tris acrylamide gels (Life Technologies) and treated with in-gel trypsin digestion[45] with minor modifications. Peptides were harvested with two extractions, first in 5% formic acid and then in 5% formic acid in 60% acetonitrile. Samples were reconstituted with 0.1% trifluoroacetic acid in 4% acetonitrile and analyzed by liquid chromatography (LC)-tandem mass spectrometry (MS/MS) with an Orbitrap Fusion Lumos Tribrid Mass Spectrometer (Thermo Electron, Bremen, Germany) online with an Ultimate 3000RSLCnano chromatography system (Thermo Fisher Scientific, Sunnyvale, CA). A detailed mass spectrometry protocol is available upon request.

Protein identification and quantification: Relative intensity-based label-free quantification (LFQ) was processed using the MaxLFQ algorithm[46] from the freely available MaxQuant computational proteomics platform[47]. Spectra were searched against a *Drosophila melanogaster* database (UniProt Proteome reference, date 2017.08; 21982 entries). The false

discovery rate (FDR) at the peptide and protein levels were set to 1% and determined by searching a reverse database. For protein grouping, all proteins that could not be distinguished based on their identified peptides were assembled into a single entry according to the MaxQuant rules. The statistical analysis was done with Perseus program (version 1.5.1.6) from the MaxQuant environment (www.maxquant.org). Quantifiable proteins were defined as those detected in at least 67% of samples in at least one condition. Protein LFQ normalized intensities were base 2 logarithmized to obtain a normal distribution. Missing values were replaced using data imputation by randomly selecting from a normal distribution centered on the lower edge of the intensity values that simulates signals of low abundant proteins using default parameters (a downshift of 1.8 standard deviation and a width of 0.3 of the original distribution). To determine whether a given detected protein was specifically differential, a two-sample t-test was done using permutation-based false discovery rate (pFDR) with a threshold at 0.1% (5000 permutations). The p-value was adjusted using a scaling factor s0=1 (Supplementary Table 1). In Figure 2, differential proteins are highlighted by a cut-off for log2|Fold change|>2 and a p-value<0.01. The mass spectrometry proteomics data have been deposited to the ProteomeXchange Consortium via the PRIDE[48] partner repository with the dataset identifier PXD017895.

Bright-field live imaging in embryos

Images of wild-type or mutant embryos were collected on an inverted microscope (Zeiss, AxioVision software) equipped with a programmable motorized stage to record different positions over time (Mark&Find module from Zeiss). Images were acquired every 2 min for 60 minutes from post dorsal movement of the posterior midgut primordium (0 min). The extent of elongation was measured by dividing the travel distance of the posterior midgut primordium at 40 min and normalized to the maximum travel distance.

RNA interference in embryos

dsRNA probes: dsRNA probes were made using PCR product containing the sequence of theT7 promoter (TAATACGACTCACTATAGG) followed by 18-21 nucleotides specific to the gene. The dsRNA probe against Toll-2 (18w, CG8896) is 393-bp long and located in the 5'UTR region (Forward primer: AGTTTGAATCGAAACGCGAGGC; Reverse primer: ATGCCAGCCACATCTTCCA). The dsRNA probe against Toll-6 (CG7250) is 518-bp long and located in the 5'UTR region (Forward primer: TCGAAAATCAGCCAACGTGC; Reverse primer: CGATTCACGGTTTAGCTGCG). The dsRNA probe against Toll-7 (CG8595) is 749-bp long and located in the coding region (Forward primer: TGGCAACCGTCTGGTTACTC; Reverse primer: CGTTCATGATGCTCTGCGTG). The dsRNA probe against Toll-8 (Tollo, CG6890) is 423-bp long and located in the 5'UTR region (Forward primer: CGTTTGTCGTTCAGCGGATG; Reverse primer: CCCCTCATAACCTCCCCGAT) and does not target the *ind-Toll-8::HA* transgenes. Gel purified PCR products were subsequently used as a template for the *in vitro* RNA synthesis with T7 polymerase using Ribomax (Promega, P1300). The dsRNA probes were purified using Sure-Clean (Bioline, BIO-37047). Triple dsRNA probes against Toll-2,6,8 and Toll-2,6,7 were prepared and injected at a final concentration of 5 µM each in RNAse-free water.

Embryo injections: Embryos were collected from fresh agar plates in cages kept at 25°C allowed for 30-min egg laying. Embryos were then dechorionated in 50% bleach, rinsed and aligned on cover slips (#1.5) covered with heptane-glue. After a few minutes of desiccation, embryos were covered with Halocarbon 200 oil and injected with dsRNA or RNase-free water. Post-injection embryos were stored at 25°C until live imaging.

Fluorescence live imaging and image processing in embryos

Embryos were aligned on cover slips (#1.5) with heptane-glue and were covered with Halocarbon 200 oil. Dual channel time-lapse imaging was performed on a Nikon Eclipse Ti inverted spinning disc microscope (Roper) with a 100x/1.4 oil-immersion objective at 22°C, controlled by the Metamorph software. Z stacks (step size: 0.5 µm) of 6~10 slices were acquired every 30 seconds, for 15~45 minutes starting from stage 6. Laser power was measured and kept constant across all experiments.

To generate 2D projections in experiments with E-Cad::GFP (Fig. 1d and Extended Data Figs. 1 and 2b), a custom FIJI macro[49] integrating the 'stack focuser' plugin from M. Umorin was used to perform maximum intensity projection for all channels with 3 Z planes around the junctional plane (labeled by E-cad::GFP). For Fig. 2b, a single plane at the junction level is manually selected based on maximum junctional sqh::GFP signals. The resulting 2D images were subjected to a background subtraction procedure using the rolling ball tool (radius 50 pixels). The 2D images were segmented on E-cad::GFP or LifeAct::Ch channels semi-automatically with manual corrections in the FIJI plug-in Tissue Analyzer[36]. The resulting segmentation masks were then dilated by 5 pixels on either side of the junction and used as masks for subsequent quantifications.

Immunofluorescence and image processing in embryos

Embryos were fixed with 8% formaldehyde for 20 min at room temperature. Embryos were processed and stained according to standard procedures[50]. Embryos were mounted in Aqua-Polymount (Polysciences). Images were acquired on a Leica SP8 inverted confocal microscope with a 63x/1.4 NA oil-immersion objective (with exception of Extended Data Fig. 4d, e acquired on a Zeiss LSM780 with a 63x/1.4 NA oil-immersion objective). Z stacks with step size of 0.25-0.4 µm were collected.

2D images were generated by maximum intensity projections followed by the same procedure as for live imaging experiments in embryos (except for 3-pixel dilatation in segmentation masks generated from β-catenin stainings).

Clonal analysis in wing discs

Flies were allowed to lay eggs in vials for ~8h at 25°C and vials were kept at 25°C until heat-shock.

For clonal overexpression of Toll-8 (Figs. 1g, 2h, 4a and Extended Data Fig. 6a) 72h AEL (after egg laying) old larvae were heat-shocked at 37° for 12 minutes and dissected after 24h.

For GAL80ts experiments (Fig. 5 and Extended Data Fig. 7), 72h AEL larvae were heat-shocked at 37° for 12 minutes, kept at 18° for 48 hours and subsequently incubated at 30°C for 2h15min in order to inactivate GAL80ts and allow expression of Toll-8::YFP.

For MARCM experiments (Mosaic Analysis with a Repressible Cell Marker, Figs. 3a-b, 4b-f and Extended Data Figs. 5, 6b-d), 72h AEL larvae were heat-shocked at 37° for 1h, kept at 18° and heat-shocked again 7 hours later at 37° for 1h. Larvae were kept at 18° for 20 hours, shifted to 25° and dissected 24h later. Keeping the larvae at 18° allowed growth of the clones in the presence of no/low levels of Toll-8 expression. Larvae to observe *cirl* mutant clones (Fig. 3d) were treated the same way.

Immunofluorescence and image processing in wing discs

Staged larvae were dissected in PBS, transferred to 4% PFA in PBS and fixed under agitation for 18 min at room temperature. After fixation, wing discs were first rinsed with PBS, then extensively washed with PBT (PBS plus 0.2% Triton-X100) and blocked in PBT with 5% normal donkey serum (NDS, Jackson Immuno Research Laboratories, 017-000-001) for at least 30 min at room temperature, followed by incubation with primary antibody in 2% NDS overnight at 4 °C. The next day wing discs were washed in PBT and incubated in secondary antibody with 2% NDS for 1h30min at room temperature. After six rounds of washes with PBT, samples were mounted in Mowiol (Sigma-Aldrich, 324590). Larval mouth hooks were used as spacers in the experiments where Myo-II was observed. Images were acquired on a Leica SP8 inverted confocal microscope with a 63x/1.4 NA oil-immersion objective. Toll-8::YFP and Sqh::Ch were visualized with their endogenous fluorescence. Image stacks with step size of 0.25-0.5 µm were collected.

Peripodial signal was masked from the image stacks in ImageJ to avoid interference with signals from the wing disc proper. 2D projections were generated using the aforementioned custom stack focuser macro in ImageJ, projecting two z planes around the junctional plane of each cell (detected by E-cad staining, except Fig. 3a, b projected on Sqh::Ch signals). This allows to project the entire wing pouch independently of the shape of the wing disc. The 2D-projected stacks were then segmented on E-cad stainings (except Fig. 3a, b segmented on Sqh::Ch signals) using Tissue Analyzer[36].

***Ex vivo* live imaging and image processing in wing discs**

The culture medium used for long-term time lapse imaging of wing imaginal disc explants is described in Dye *et.al.*[27]. In short, Grace's insect medium (Sigma G9771, without sodium bicarbonate) was buffered with 5mM BisTris and the pH adjusted to 6.6-6.7. Subsequently the medium was sterile filtered (0.2µm pore size) and kept at 4°C for up to 4 weeks. At the day of the experiment the medium was supplemented with 5% fetal bovine serum (FBS), Penicillin-Streptomycin (final 1x from a 100x stock solution, Sigma P4333) and warmed to 30°C in a water bath. Just before dissection of the larvae, 20-Hydroxyecdysone (20E, Sigma, H5142) was added to yield a total concentration of 20nM. 20E was kept as a 1000x stock solution in ethanol at -20°C. For the experiment, 72h AEL larvae were heat-shocked at 37° for 12 minutes, kept at 18° for 48 hours and subsequently incubated at 30°C for 2h15min in a water bath. Subsequently,

larvae were floated out of the food using 30% glycerol and washed in sterile water twice. Surface sterilization in 70% Ethanol was followed by another wash in sterile water and then in medium. Larvae were dissected in culture medium, wing discs isolated and mounted on a round cover slip. In order to restrict disc movement during imaging, discs were covered by a porous membrane (Whatman cyclopore polycarbonate membranes; Sigma, WHA70602513) using two stripes of double-sided tape as spacers. Finally, this sandwich was mounted in an Attofluor cell chamber (A7816, Invitrogen) and filled with 1ml of medium and covered with Parafilm M (P7793, Sigma-Aldrich) to avoid evaporation. Discs were imaged on a Nikon Eclipse Ti inverted spinning disc microscope (Roper) equipped with an incubation chamber heated to 30°C. Imaging was done using a 60x/1.2 NA water-immersion objective (Fig. 5a, Extended Data Fig. 7a and Movie 1 and 2) or a 100x/1.4 NA oil-immersion objective (Movie 3 and 4). Dual imaging of Toll-8::YFP and Sqh::Ch was performed by simultaneous excitation of fluorophores with 515nm and 561nm laser lines using a dichroic mirror to image on two cameras (Evolve 512, Photometrics). Stacks of 40 slices with 0.7µm spacing were acquired every 10min (60x movies) or every 5min (100x movies).

A maximum projection of the disc proper junctional plane was obtained by masking the peripodial epithelium and the lateral portion of the disc proper manually in ImageJ based on sqh::Ch signals. Background subtraction was done using a rolling ball (50px radius) in ImageJ.

Data analysis

Definition of expression interfaces: When references channels (Toll-8::HA, Toll-8::YFP, Toll-8::GFP, or LacZ staining) were available, expression interfaces were defined from reference channels in Tissue Analyzer.
To define horizontal cell rows in Fig. 1d and Extended Data Fig. 2b, cell rows were counted from the ventral midline, with the 4th cell row (most ventral) being 2 rows away from the ventral midline. The border between the 2nd and the 3rd cell rows is consistent with the position of *ind* ventral expression border.
To define vertical cell columns in Extended Data Fig. 1, parasegment boundaries were visualized with Eve::YFP, with the anterior boundary of Eve::YFP signal defined as the parasegment boundary between even- and odd-numbered parasegments. Thus, cell columns 1-4 belong to odd-numbered parasegments (Eve::YFP+), while 5-8 belong to even-numbered parasegments (Eve::YFP-).

Quantification of junctional Myo-II intensities: Raw pixel intensities from segmented junctions were measured in Tissue Analyzer. To extract data tables containing raw pixel intensities from Tissue Analyzer, a customized R procedure was developed using the RSQLite package. Adjusted junctional pixel intensities were obtained by subtracting mean cytoplasmic intensity value measured on each image. Enrichment was calculated as ratios of adjusted junctional intensity values between junctions of interest and those in nearby wild-type tissues (Extended Data Fig. 2a).

Quantification of border smoothness: Boundary smoothness for ventral *ind* expression border in the embryo was calculated as the ratio between distance between two end vertices over total junctional length (Extended Data Fig. 2a, left). Border smoothness value approaches 1 as the border gets smoother.

For clone smoothness in the wing disc, an original method developed by P. Villoutreix (Centuri, France) was implemented in Tissue Analyzer by B. Aigouy (IBDM, France) under the plugin 'Clone wiggliness'. In brief, the boundary of the clone was extracted, the vertices present at the clone boundary were ordered, and an angle was calculated for each vertex with its two neighboring vertices present at the clone boundary (Extended data Fig. 2a, right). A mean value per clone was then calculated and this value is getting closer to 180° if the clone is smooth.

Quantification Toll-8 planar-polarity (Fig. 5d): We restricted our analysis to single cells expressing low Toll-8::YFP levels in the vicinity of a high Toll-8::YFP expressing cell. This ensured that each junction included in our computation only contained Toll-8::YFP originating from the single cell that was quantified. For each single cell, junctional Toll-8::YFP levels were extracted (using the segmented line tool in ImageJ, line width = 6px) along the parallel junctions (Toll-8$^{\parallel}$, the junctions not being in contact with the high Toll-8 expressing cell) and along the two junctions being in direct contact with high Toll-8 expressing cell (Toll-8$^{\perp}$). Toll-8::YFP enrichment at parallel junctions was computed by calculating the ratio between mean Toll-8$^{\parallel}$ and mean Toll-8$^{\perp}$ levels (Fig. 5d, scheme).

Data visualization: With the exception of Extended Data Fig. 7a, data visualization was performed in R with customized scripts. The following custom packages were used: "fields" and "ggplot2". Intensity profiles shown in Extended Data Fig. 7a were plotted in Phython using the Seaborn library.
Box-plot elements are defined as follows: center line represents the median; box limits represent the first and third quartiles (the 25th and 75th percentiles); upper whisker extends from the box limit to the largest value no further than 1.5x interquartile range from the box limit and lower whisker extends from the box limit to the smallest value at most 1.5x interquartile range from the box limit; all data points are plotted on the graph.

Statistics

All P values were calculated using the Mann-Whitney U test in R. No statistical method was used to predetermine sample size. The experiments were not randomized, and the investigators were not blinded to allocation during experiments and outcome assessment.

Repeatability

All measurements were performed in 8–100 independent experiments. Each embryo and clone in the wing disc is considered as an independent experiment.

Data Availability

The authors declare that the data supporting the findings of this study are available within the paper and its supplementary information files. Raw image data are available upon reasonable request.

Code availability

The custom R and Python codes used to perform image analysis are available upon request.